Nikoukar Romina (Orcid ID: 0000-0002-8608-2822)
Lawrence David, J. (Orcid ID: 0000-0002-7696-6667)
Peplowski Patrick, N (Orcid ID: 0000-0001-7154-8143)
Dewey Ryan, M. (Orcid ID: 0000-0003-4437-0698)
Korth Haje (Orcid ID: 0000-0001-7394-7439)
Baker Daniel, N. (Orcid ID: 0000-0001-5909-0926)
McNutt Ralph, L. (Orcid ID: 0000-0002-4722-9166)

Statistical Study of Mercury's Energetic Electron Events as Observed by the Gamma-Ray and Neutron Spectrometer Instrument onboard MESSENGER

Romina Nikoukar[1], David J. Lawrence[1], Patrick N. Peplowski[1], Ryan M. Dewey[2], Haje Korth[1], Daniel N. Baker[3], Ralph L. McNutt Jr. [1]

[1]Johns Hopkins University Applied Physics Laboratory, Laurel, MD, USA.

[2]Department of Climate and Space Sciences and Engineering, University of Michigan, Ann Arbor, MI, USA.

[3]Laboratory for Atmospheric and Space Physics, University of Colorado, Boulder, CO, USA.

Corresponding author: Romina Nikoukar (romina.nikoukar@jhuapl.edu)

Key Points:

- A comprehensive survey of energetic electron (EE) events observed with the Neutron Spectrometer (NS) and the Gamma-Ray Spectrometer anticoincidence shield (ACS) is conducted.
- The majority of EE events detected in the NS are also detected in the ACS and appear to be comprised of gyrating, drifting electrons.
- ACS-only and ACS-enhanced events exhibit a significantly different spatial and temporal characteristics compared with the other EE event classes.

This is the author manuscript accepted for publication and has undergone full peer review but has not been through the copyediting, typesetting, pagination and proofreading process, which may lead to differences between this version and the Version of Record. Please cite this article as doi: 10.1029/2018JA025339

Abstract

We present results from a statistical analysis of Mercury's energetic electron (EE) events as observed by the Gamma-Ray and Neutron Spectrometer instrument onboard the MESSENGER spacecraft. The main objective of this study is to investigate possible anisotropic behavior of EE events using multiple data sets from MESSENGER instruments. We study the data from the Neutron Spectrometer (NS) and the Gamma-Ray Spectrometer (GRS) anticoincidence shield (ACS) because they use the same type of borated plastic scintillator and hence they have very similar response functions, and their large surface areas make them more sensitive to low-intensity EE events than MESSENGER's particle instrumentation. The combined analysis of NS and ACS data reveal two different classes of EEs; "Standard" events and "ACS-enhanced" events. Standard events, which comprise over 90% of all events, and have signal sizes that are the same in both the ACS and NS. They are likely gyrating particles about Mercury's magnetic field following a 90-degrees pitch angle distribution and are located in well-defined latitude and altitude regions within Mercury's magnetosphere. ACS-enhanced events, which comprise less than 10% of all events, have signal sizes in the ACS that are 10 to 100 times larger than those observed by the NS. They follow a beam-like distribution, and are observed both inside and outside Mercury's magnetosphere with a wider range of latitudes and altitudes than Standard events. The difference between the Standard and ACS-enhanced event characteristics suggests distinct underyling acceleration mechanisms.

1. Introduction

Mariner 10 observed transient bursts of energetic particles in Mercury's magnetosphere during its three flybys of Mercury in the early 1970s [*Simpson et al.* 1974]. Specifically, *Simpson et al.* [1974] reported detection of energetic protons with energies of ~550 keV and energetic electrons of ~300 keV within Mercury's magnetosphere. A later study by *Armstrong et al*. [1975, 1979] suggested that the Mariner 10 energetic particle instruments were likely responding to pulse pile-up from low-energy (~35-175 keV) electrons rather than more energetic electrons or ions. This issue was not resolved until shortly after the insertion of the MErcury Surface, Space ENvironment, GEochemistry, and Ranging (MESSENGER) spacecraft into its Mercury orbit, when data from the Energetic Particle Spectrometer (EPS) demonstrated that the primary energetic particles within Mercury's magnetosphere are electrons and not protons [*Ho et al.*, 2011(a), (b)]. In a subsequent study, *Ho et al.* [2012] reported the spatial distribution of 51 energetic electron (EE) events based on the observations from a full year of MESSENGER's primary orbital mission phase. They found that most of the intense, moderate-energy (tens to hundreds of keV) electron events occured either at local midnight or at high northern latitudes.

It was discovered early in the orbital mission that three other instruments on the MESSENGER spacecraft – the Neutron Spectrometer (NS), the Gamma-Ray Spectrometer (GRS), and the X-Ray Spectrometer (XRS) – also responded to energetic electrons, and provided highly sensitive, time-resolved measurements of energetic electron bursts [*Ho et al.*, 2011(a)]. Because the sensor

area of these instruments was significantly larger than that of the EPS [*Goldsten et al.*, 2007], the NS, GRS, and XRS were over an order of magnitude more sensitive than the EPS for detecting energetic electrons. For the GRS, both the main Ge gamma-ray sensor and the scintillator anticoincidence shield (ACS) were sensitive to EE events. In addition, a subset of the NS and GRS datasets were acquired at significantly shorter (1 s for the NS and 10 ms for the GRS) acquisition intervals than the EPS (3 s) or XRS (20 s). Such high-time-resolution capabilities are critical for characterizing charged-particle measurements at Mercury, where the characteristic timescales are as short as a few seconds [*Slavin et al.*, 2010; *Dewey et al.*, 2017]. Based on their sensitivity and timing characteristics, the combined NS and GRS measurements provide an optimum sensitivity and time resolution for characterizing Mercury's energetic electrons.

Lawrence et al. [2015] carried out a comprehensive survey of EE events using 30 months of continuously recorded NS data. This study showed that while Mercury does not have a trapped population of energetic particles, the stochastically timed occurrences of EE events are located in well-defined regions and form "quasi-permanent structures" within Mercury's magnetosphere. The *Lawrence et al.* [2015] study identified over 2700 electron burst events and showed their temporal, spatial, and spectral behavior. In a subsequent study, *Baker et al.* [2016] investigated the most intense energetic electron events among the GRS high-resolution measurements and found signatures of accelerated electrons being injected from the near-tail region and forming quasi-trapped populations. *Gershman et al.* [2015] also observed that during solar energetic particle events there are enhanced electron fluxes within the central plasma sheet that are indicative of an apparent trapped electron population at low latitudes in the magnetotail. *Ho et al.* [2016] presented XRS observations of low-energy (1-10 keV) or suprathermal electrons, where 3102 events were identified during 3900 orbits around Mercury, sampling all Mercury longitudes multiple times over a four-year period. *Dewey et al.* [2017] studied energetic electron acceleration and injection mechanisms during dipolarization events using the GRS high-time-resolution data and concluded that, while ~25% of energetic electron events in Mercury's magnetotail were directly associated with dipolarization, the remaining events were consistent with the near-Mercury neutral line model of magnetotail injection and eastward drift as suggested in [*Baker et al.*, 1986, 1987, 1996, 2016, *Russel et al.*, 1988], and that electrons might participate in Shabansky-like closed drifts about the planet [*Walsh et al.*, 2013]. As electrons drift about the planet, they are continually lost via surface precipitation [*Starr et al.*, 2012] and magnetopause shadowing [*Lindsay et al.* , 2016].

In this study, we carry out an analysis of EE events measured with the GRS ACS (abbreviated hereafter as ACS) that is analogous to the analysis of NS data carried out by *Lawrence et al.* [2015]. Based on this analysis, we then characterize EE events observed by both the NS and ACS to investigate possible anisotropic behavior of EE events. While both NS and ACS are sensitive to bremsstrahlung photons produced when energetic electrons impact materials located near the respective sensors [*Lawrence et al.*, 2015], they were located on different sides of the MESSENGER spacecraft, and thus may have different sensitivities to directional EE events. In Section 2, we present a brief description of the two sensors, the data used in this study, and the

EE event detection and classification. Section 3 presents the results of the statistical analyses. We discuss the implication of our findings in Section 4 and present a summary in Section 5.

2. EE Observations

2.1 Gamma-Ray and Neutron Spectrometer

The NS sensor is located on the side of the spacecraft opposite to the spacecraft's sunshade (+*y* in spacecraft-fixed Cartesian coordinates). The NS consists of three scintillators that separately measure thermal, epithermal, and fast neutrons through a combination of spacecraft Doppler and coincidence pulse processing techniques [*Goldsten et al.*, 2007, *Lawrence et al.*, 2013]. The central NS sensor is a 10 x 10 x 10 cm^3 cube of borated plastic (BP) scintillator (BC 454) that has omnidirectional response to epithermal and fast neutrons. Because of the large volume of the BP sensor, it has a high sensitivity to EE events and as a result, the data from this sensor provides the NS-based EE event data set for this study. The NS operates in three modes: near-planet (altitude less than 7000 km), far-planet (altitude greater than 7000 km), and burst. The NS was operated with accumulation times of 20 s, 300 s and 1 s for the near-planet, far-planet, and burst modes, respectively [*Lawrence et al.*, 2015]. The near-planet mode accumulation time (20 s) is short enough to study the energetic events, and the data from this mode is used in this study. The BP pulse height spectra are divided into 64 channels whose values are non-linearly proportional to the energy deposited in the BP. Pulse height spectra are hereafter referred to as energy spectra for simplicity.

The GRS system consists of two sensors: a high purity germanium (HpGe) gamma-ray sensor, which was cryocooled and was sensitive to gamma rays from 50 keV to 10 MeV, and a borated plastic ACS to actively reject background charged particles from the germanium detector [*Goldsten et al*., 2007]. The ACS is sensitive to electrons with energies greater than 50 keV up to several hundred keV through bremsstrahlung photon production by impact of energetic electrons on the sensor housing and nearby material [*Lawrence et al.*, 2015]. When the GRS cryocooler stopped operating on 5 June 2012 after 9500 hours of operation [*Evans et al*., 2017], the GRS flight software was reconfigured on 25 February 2013 to optimize ACS measurements of EE events and planetary neutrons [*Peplowski et al*., 2015; *Evans et al*., 2017]. Moreover, the GRS operating modes were modified to be similar to those of the NS with a near-planet accumulation time of 20 s. The far-planet time cadence was set to 1800 s. Like the BP sensor, the ACS data are pulse height (energy) spectra divided into 1024 channels.

The ACS is located on the main instrument deck of the spacecraft (+*z* in spacecraft-fixed Cartesian coordinates) [*Peplowski et al.*, 2015]. Because of the similarity in the sizes of the NS and ACS borated plastic sensors, the data provide similar time-resolved data sets. Meanwhile, the different locations of the NS and the ACS on the spacecraft can provide some directional information on EE events.

2.2 Data

This study focuses on the data collected by NS and ACS between 1 March 2013 and the end of the MESSENGER mission (30 April 2015). This period is after the GRS flight software update that improved the sensitivity to EEs. This period also includes a new phase of the MESSENGER orbital mission starting in April 2012 when the apoapsis of the spacecraft orbit was reduced from 15,000 km to ~10,000 km, reducing the orbital period from 12 h to 8h [*Lawrence et al.*, 2015, *Baker et al.*, 2016]. Note that the GRS flight software reconfiguration also included the addition of the high-time-resolution (10 ms) mode for measurements of energetic electrons. In this study, however, we focus on the 20-s accumulation time data from both the NS and the ACS excluding the far-planet mode data and altitudes greater than 4000 km. The periods of solar energetic particle (SEP) events as identified by *Lawrence et al.* [2016] are also excluded from this study. A complementary study of ACS 10-ms data was conducted by *Dewey et al*. [2017].

2.3 EE Event Detection

Figure 1(a) shows an example of ACS count rate data with 20-s sampling time. The slowly varying temporal profile is due to the changing solid-angle subtended by Mercury as viewed by the ACS. The energetic electron event is recognized as the deviation from the nominal solid angle dependence of the count rate data. This deviation is more pronounced in the low-energy count-rate data (channels 0 to 19) and is nearly absent in the high-energy (channels 700 to 1023) count-rate data as shown in Figure 1(b) and 1(c). Both low-energy and high-energy count rate time profiles exhibit a similar solid angle dependence. We use this characteristic to devise an EE event detection procedure for ACS data similar that used by *Lawrence et al.* [2015].

The detection algorithm consists of the following steps. The high-energy counts are first low-pass filtered using a boxcar function of length 100 s. The filtering is necessary to reduce the noise. Low-energy counts with values less than an orbit-specific threshold are fit to the filtered high-energy counts ($\boldsymbol{C_{high}}$). The threshold is set relative to the median of the counts for each orbit and is chosen to be sufficiently large to include all the background counts and small enough to exclude the EE-related counts from the fitting. An example of such linear fit is shown in Figure 1(d). The modeled low energy counts ($\boldsymbol{C_{low,model}}$) can be written as

$$\boldsymbol{C_{low,model} = \alpha C_{high} + \beta}$$

where $\boldsymbol{\alpha}$ and $\boldsymbol{\beta}$ are the coefficients of the linear fit. The temporal profile of the modeled low energy counts is shown in blue in Figure 1(b). The signal-to-noise ratio (SNR), which we use as a measure for EE detection, is defined as the difference between the actual and modeled low energy counts as

$$\boldsymbol{SNR = (C_{low} - C_{low,model}) / \sigma_{50th}}$$

where $\boldsymbol{C_{low}}$ represents the low energy counts, and $\boldsymbol{\sigma_{50th}}$ is the standard deviation of the lower 50th percentile ACS count rate for the corresponding orbit. Figure 1(e) shows the SNR time

profile for the ACS data orbit #1962. The candidate EE events are identified with SNR greater than a threshold level (≥ 4). Note that *Lawrence et al.* [2015] use the fast neutron counts as the basis of the linear fit for the NS data with a threshold value of 5. The threshold value that we chose for the GRS is based on the visual inspection for EE events that are identified in both the NS and GRS ACS data. As an additional criterion, we require at least 2 adjacent data points with SNR > 4 within each event unless the SNR is large (> 9). Once the counts above the threshold are identified, we expand the events to include SNR greater than 2 at both start and end of the events. If the events are separated by less than 60 s, they are joined together and counted as one. The data from 9 May 2013 shows one EE event identified by red diamonds in Figure 1(b) and 1(e).

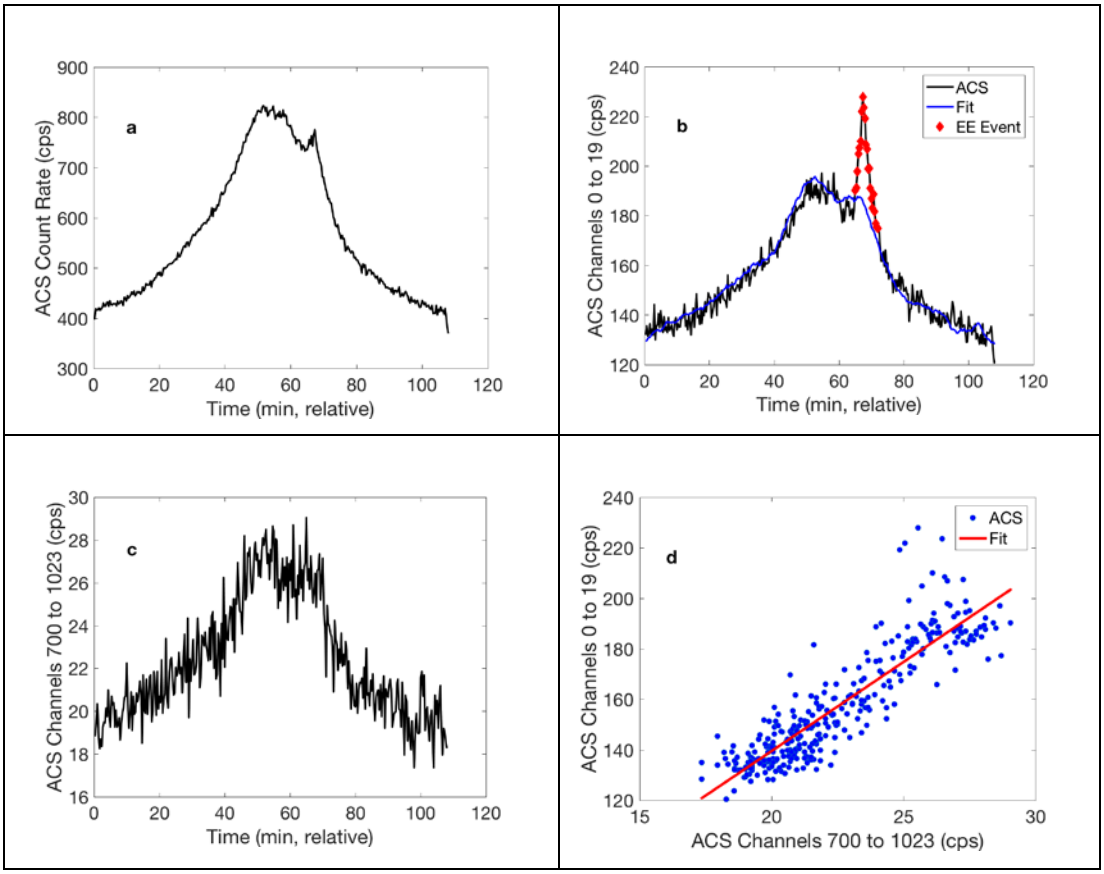

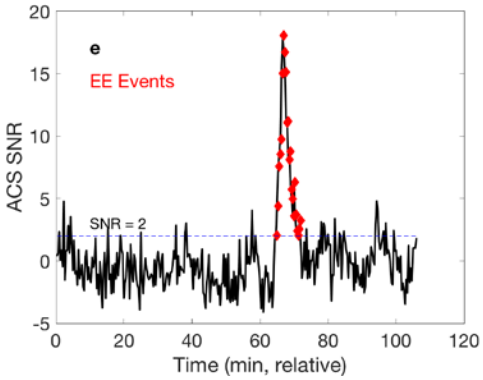

Figure 1. An example of an EE event detected by ACS on 9 May 2013 between 16:42 UT and 16:50 UT. (a) The ACS count rate data for the near-planet portion of orbit 1962. (b) The ACS low-energy channel count rate data and the fit of ACS low-energy channel data to high-energy channel data are shown in black and blue lines, respectively. The EE event is marked in red diamonds. (c) The ACS high-energy channel count rate data. (d) Low-energy channel data vs high-energy channel data for the same period of Figure 1(a). Individual data points are plotted in blue circles, while the linear fit is plotted in red. e) The ACS SNR for the data during the same period. The EE event is plotted in red diamonds. The dashed line shows the SNR = 2 threshold.

2.4. EE Event Classification

The aim of this work is to conduct a comparative study of EE events detected by the NS and GRS ACS. Therefore, we first classify the EE events in four classes: 1) "Coincident" events: EE events detected by both the NS and ACS either at the same time or with some overlap. 2) "NS-only" events: EE events detected exclusively in the NS data. 3) "ACS-only" events: EE events detected exclusively in the ACS. 4) "ACS-enhanced" events: these are EE events where the ACS shows enhanced SNR compared to the same events seen in the NS. The characteristics of these classes are further described in Section 3.

We also consider the smooth versus bursty classification defined by *Lawrence et al.* [2015] to focus on individual EE events detected by individual sensors. To quantify the measure of smoothness, they define two parameters, $\boldsymbol{I_{norm}}$ and $\boldsymbol{\sigma_{filter\ ratio}}$ as follows.

$$\boldsymbol{I_{norm}} = \frac{\sum_{i=1}^{D}(\boldsymbol{SNR})_i}{\boldsymbol{D}*(\boldsymbol{SNR})_{max}} \quad (1)$$

$$\boldsymbol{\sigma_{filter\ ratio}} = \boldsymbol{\sigma}\left(\frac{(\boldsymbol{SNR})_i}{\boldsymbol{B}[\boldsymbol{SNR_i},\boldsymbol{w}]}\right) \quad (2)$$

D is the event length, $(\boldsymbol{SNR})_{\boldsymbol{i}}$ and $(\boldsymbol{SNR})_{\boldsymbol{max}}$ are the SNR at the *i*th point of the event and maximum SNR of the entire EE event. We note that the term *D* in the denominator needed for normalization is missing from equation (2) in [*Lawrence, et al*. 2015]. $\boldsymbol{B}[(\boldsymbol{SNR})_{\boldsymbol{i}}, \boldsymbol{w}]$ is *i*th point of the filtered SNR with a boxcar function with length *w*. $\boldsymbol{I_{norm}}$ is basically a magnitude-normalized time integral varying between 0 and 1. $\boldsymbol{\sigma_{filter\ ratio}}$ is the standard deviation of the quotient of the SNR and low-pass-filtered ratio. Smooth events in general have higher values of $\boldsymbol{I_{norm}}$and lower values of $\boldsymbol{\sigma_{filter\ ratio}}$.

3. EE Events: Statistical Analyses

This section presents results of statistical analyses that were conducted on the EE events detected from both the NS and GRS ACS sensors. These analyses include investigations of EE-event intrinsic characteristics, geographical locations, energy spectra, and spacecraft location and orientation with respect to Mercury's magnetospheric magnetic field. The data were taken between 1 March 2013 and 30 April 2015. In this time interval, 1960 EE events were detected by the NS while 1291 EE events were detected by the ACS.

3.1 Statistical Analysis: Intrinsic Characteristics

Figure 2 shows a scatter plot of the maximum SNR ($\boldsymbol{SNR_{max}}$) of the ACS-detected EE events versus $\boldsymbol{SNR_{max}}$ of the NS events, where the four event classes (Coincident, NS-only, ACS-only, and ACS-enhanced) are illustrated. ACS-only, NS-only, and Coincident events are shown in Figure 2(a); ACS-enhanced events are shown in Figure 2(b). Table 1 provides a percentage breakdown for total EE events by sensor, and for the four different classes. Coincident events (circles in Figure 2(a)) are those events that are detected in both the ACS and NS. The sharp cutoff along the NS and ACS axes at values of 5 and 4, respectively, denote the threshold levels that were used for the NS and ACS event detection. Coincident EE events detected by the NS show a slightly higher maximum SNR than the ones detected by the ACS. A linear fit of $\boldsymbol{SNR_{max}}$ for the ACS versus that of the NS is shown by the red line in Figure 2(a). The slope of the line is 0.97, which indicates that for Coincident events, the $\boldsymbol{SNR_{max}}$ values are very similar. The dashed black and green lines in Figure 2(a) show the one-standard-deviation (σ) boundary of the data-point residual with respect to the linear fit.

Event Type	**Number of Events**	**Percentage of Total**
Event totals		
Total	2061	100%
ACS Total	1291	63%
NS Total	1960	95%
Event classes		
ACS-only class	101	5%
NS-only class	770	37%
Coincident class	1190	58%

ACS-enhanced class	147	7%

Table 1. Breakdown of ACS and NS total events and event classes.

A few conclusions can be drawn from the distribution and boundaries shown in Figure 2(a). First, the observation that approximately 35% fewer EE events were detected by the ACS compared to the NS (even with a lower SNR threshold) shows that the overall efficiency of the ACS for detecting EE events is smaller than the NS. This may be due, in part, to the less uniform geometry of the ACS compared to the NS. Specifically, the ACS is composed of two pieces of scintillator – an annulus and a puck – that are connected by a transparent light pad. *Peplowski et al*. [2015] showed that the light output of the two detector components is different due to their different geometries. In contrast, the NS is a single 10cm x 10cm x 10cm block. Although the ACS appears to have a lower efficiency for detecting EE events, most of the events seen by ACS are also seen by the NS with a similar sized signal (1190 out of 1291, or 92%). Thus, for almost all events large enough to be seen by both sensors, both observe similar sized signals. This observation, combined with information regarding magnetic field orientations, will be used to suggest that the electrons detected during Coincident events are aligned perpendicular to magnetic field lines.

The distribution in Figure 2(a) also suggests the definition of the fourth event class, namely ACS-enhanced events. ACS-enhanced events (black crosses in Figure 2(b)) are those that lie above the primary trend line with ACS $\boldsymbol{SNR_{max}}$ values notably larger than the NS. As will be shown, these ACS-enhanced events have similar characteristics as the ACS-only events, and thus likely represent a single population of events different from Coincident events.

To classify the events as smooth and bursty, we use the same thresholds for $\boldsymbol{I_{norm}}$ and $\boldsymbol{\sigma_{filter\ ratio}}$ as in *Lawrence et al*. [2015]. Because $\boldsymbol{SNR_{max}}$ is slightly different for the NS and ACS events, the smoothness parameters will not be the same (even for Coincident events), and hence this classification is performed on events of each instrument separately. Events with $\boldsymbol{I_{norm}}$ > 0.38 and $\boldsymbol{\sigma_{filter\ ratio}}$ < 0.8 are classified as smooth events. For Coincident events, however, in order to have a more robust classification algorithm, we impose an additional criterion that the $\boldsymbol{I_{norm}}$ for the NS and the ACS be within 0.1 from one another. Therefore, if a Coincident event in one sensor has an $\boldsymbol{I_{norm}}$ slightly less then threshold, but has an $\boldsymbol{I_{norm}}$ greater than threshold for the other sensor, it is classified as a smooth event.

Histograms of the event duration for each class (Coincident, NS-only, ACS-only, and ACS-enhanced) are shown in Figure 3. Histograms of smooth and bursty EE events are also plotted. While Coincident events span a wide range of durations from one minute to twenty minutes, the majority of NS-only events have durations of 10 minutes or less with smooth characteristics. The ACS-only and ACS-enhanced events have typically much shorter duration (about two minutes), and their majority have bursty characteristics. In Section 4, using the magnetic field information,

we suggest that this short duration and the associated bursty behavior is more consistent with the ACS events following a beam-like distribution.

Histograms of $\boldsymbol{SNR_{max}}$ values are shown in Figure 4. Because the $\boldsymbol{SNR_{max}}$ values are slightly different in the NS and the ACS, we separate the Coincident events with two histograms. Similar to event duration, the Coincident events show a larger dynamic range for both the NS and ACS maximum SNR, varying mainly from 5 to about 2000. The NS-only events have smaller $\boldsymbol{SNR_{max}}$ values, while the ACS-only and ACS-enhanced events have $\boldsymbol{SNR_{max}}$ values as high as 200, and 2000, respectively. The histograms follow a power-law distribution for all event classes. The power-law distribution is steepest for NS-only events and less steep for the Coincident events. A majority of ACS-enhanced events are categorized as bursty (red circles in Figure 2(b)) due to their high SNR and shorter duration.

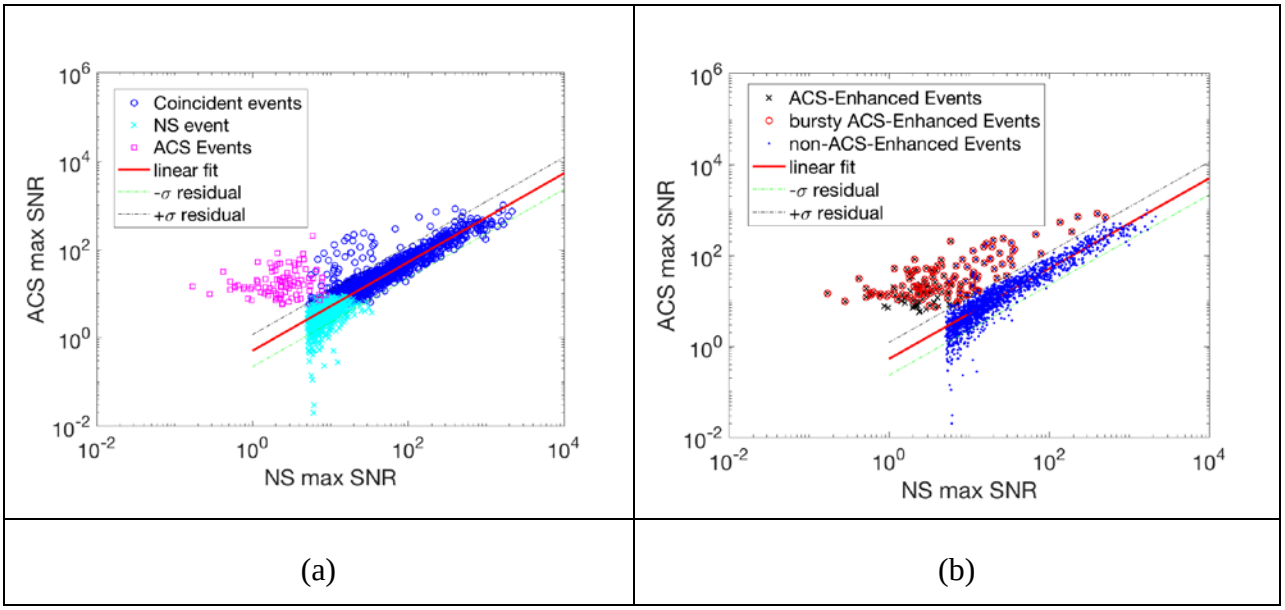

(a) (b)

Figure 2. (a) ACS $(\boldsymbol{SNR})_{\boldsymbol{max}}$ vs NS $(\boldsymbol{SNR})_{\boldsymbol{max}}$ for all the EE events detected between 1 March 2013 and 30 April 2015. Coincident events are shown in circles, NS-only events are shown by crosses, and ACS-only events are shown by squares. The red line shows a linear fit of the SNR_{max} for ACS versus that of the NS for Coincident events. The dashed lines show one-standard deviation (σ) from the linear fit. (b) ACS-enhanced events, which lie above the black dashed line, are denoted by black crosses. Red circles show bursty events in this class. The non-ACS-enhanced events are shown in blue dots.

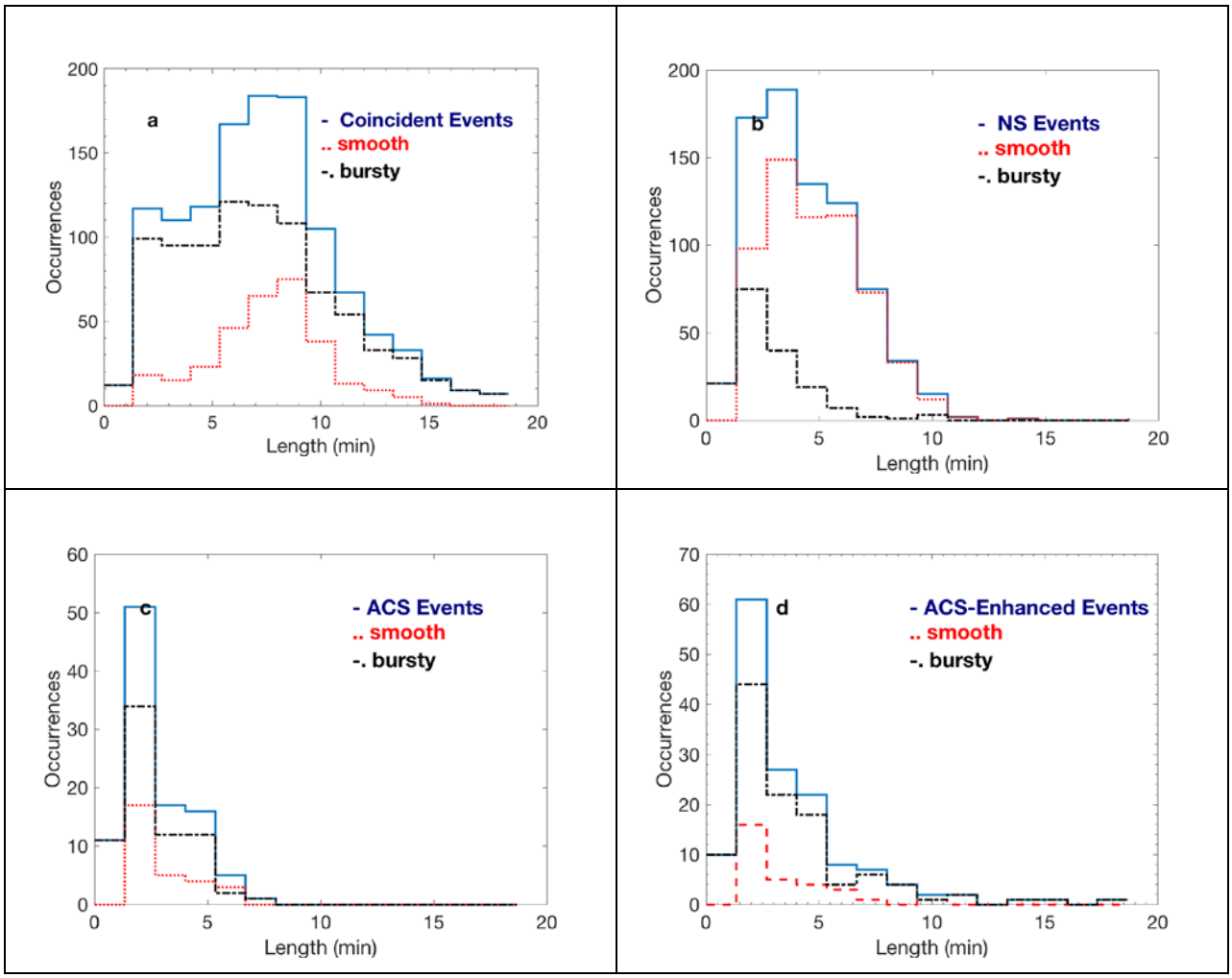

Figure 3. Histograms of the EE-event duration for (a) Coincident; (b) NS-only; (c) ACS-only; and (d) ACS-enhanced. Histograms of smooth and bursty events are shown in red and black, respectively, for each class.

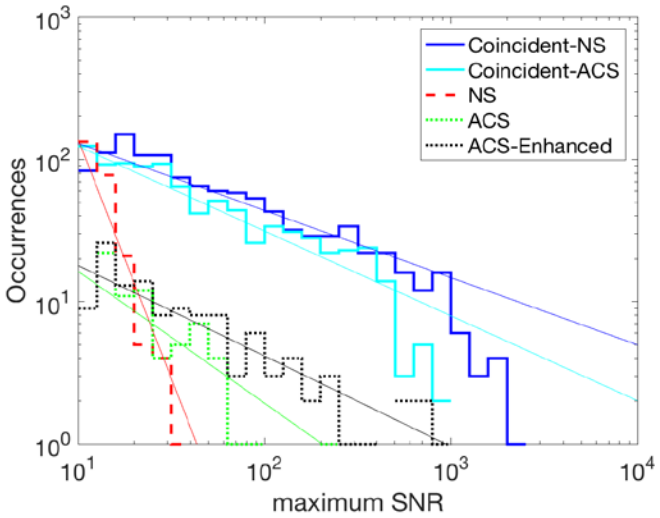

Figure 4. Histograms of maximum SNR for Coincident events. NS values and ACS values for Coincident events are plotted in blue and cyan, respectively; red and green traces show histograms of NS-only and ACS-only events. All histograms follow a power-law distribution (thin lines) with power law indices of -0.47 ± 0.11, -0.59 ± 0.08 , -3.36 ± 0.4, -0.92 ± 0.38, -0.63 ± 0.23 for Coincident (NS), Coincident (ACS), NS-only, ACS-only, and ACS-enhanced, respectively.

3.2 Statistical Analyses: Geographical Location

Figures 5, 6, and 7 show histograms of latitude, altitude, and local time, respectively, for events from each of the Coincident, NS-only, ACS-only, and ACS-enhanced classes. Each histogram has been normalized by the phase-space coverage in latitude, altitude, and local time of the spacecraft for the period used for this study. The normalization is applied by dividing each histogram by the histogram of the satellite coverage for the whole period of study and multiplying by 100 to achieve percentages. Coincident and NS-only events are mainly detected in the northern hemisphere with latitudes less than 50°N. However, ACS-only and ACS-enhanced events are more widely distributed across all latitudes. The altitude distribution for Coincident and NS-only events peaks around 700 km (more than 95% of these events occur at altitudes below 2000 km from Mercury), whereas ACS-only and ACS-enhanced events are more uniformly distributed with a distinct peak at 2700 km. Note that in terms of event locations, latitude and altitude are not independent parameters as the MESSENGER eccentric orbit does not cover all portions of the latitude-altitude phase space.

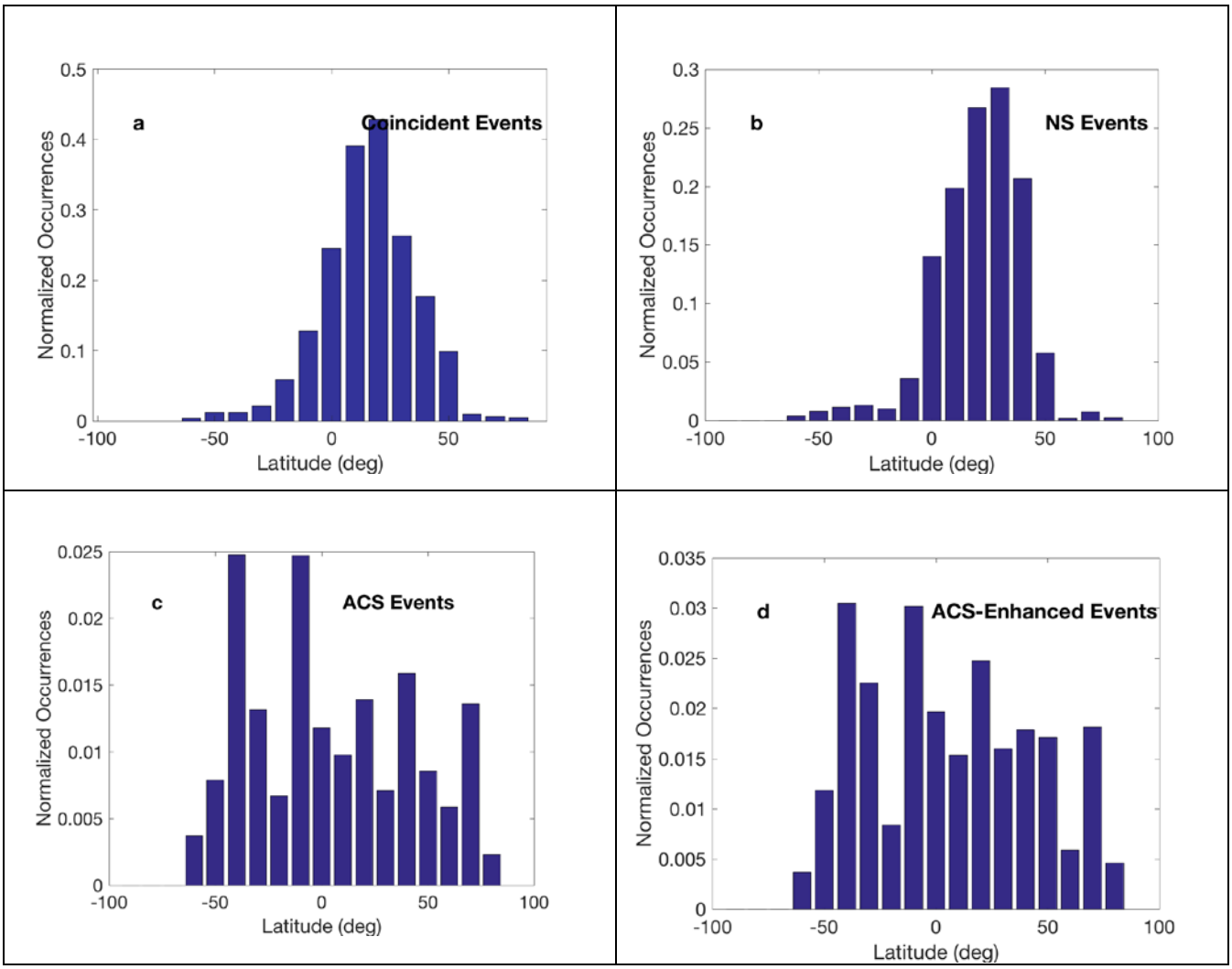

Figure 5. Normalized occurrences of events binned by latitude. (a) Coincident events; (b) NS-only events; (c) ACS-only events; and (d) ACS-enhanced events.

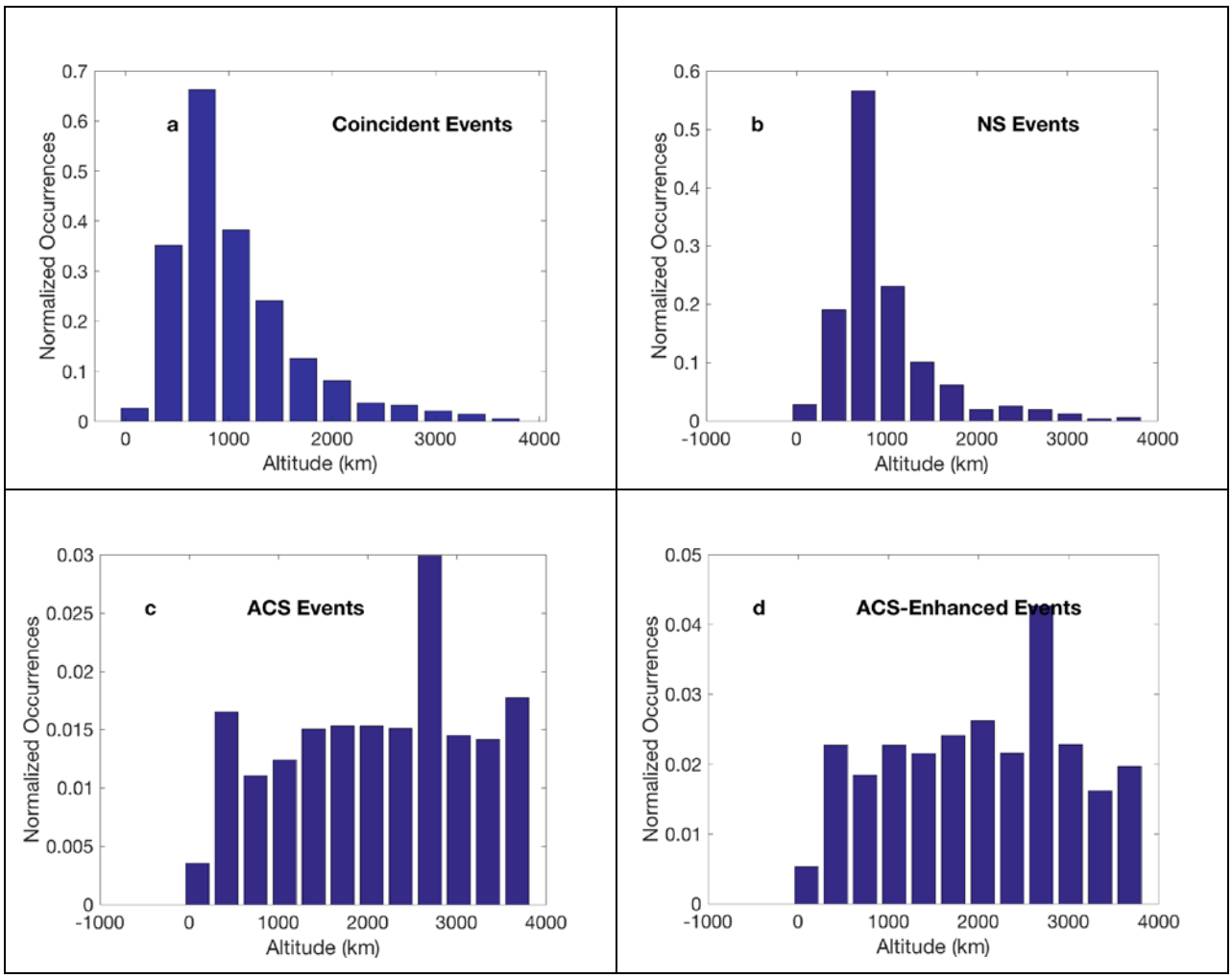

Figure 6. Normalized occurrences of events binned by altitude. (a) Coincident events; (b) NS-only events; (c) ACS-only events; (d) ACS-enhanced events.

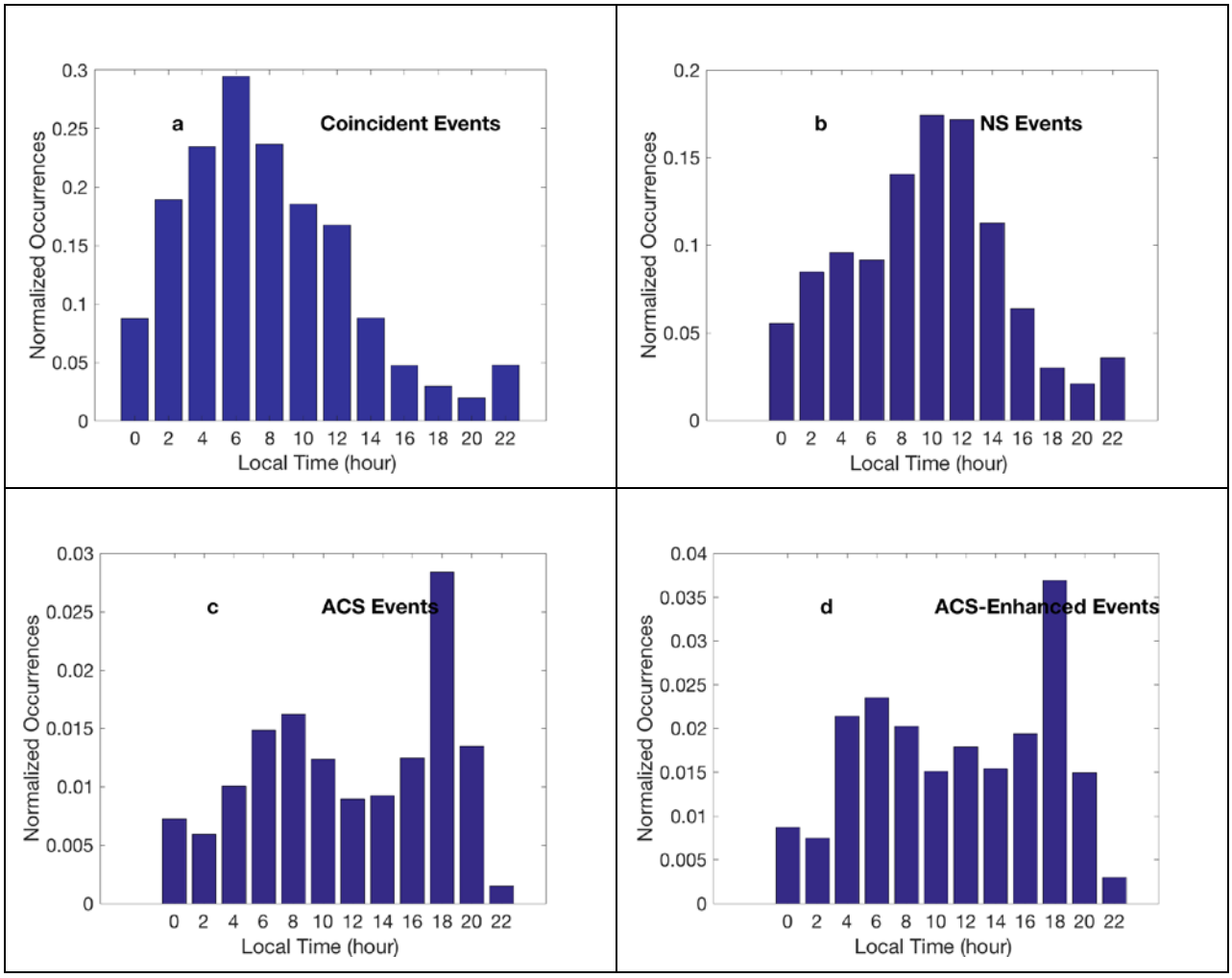

Figure 7. Normalized occurrences of events binned by local time. (a) Coincident events; (b) NS-only events; (c) ACS-only events; (d) ACS-enhanced events.

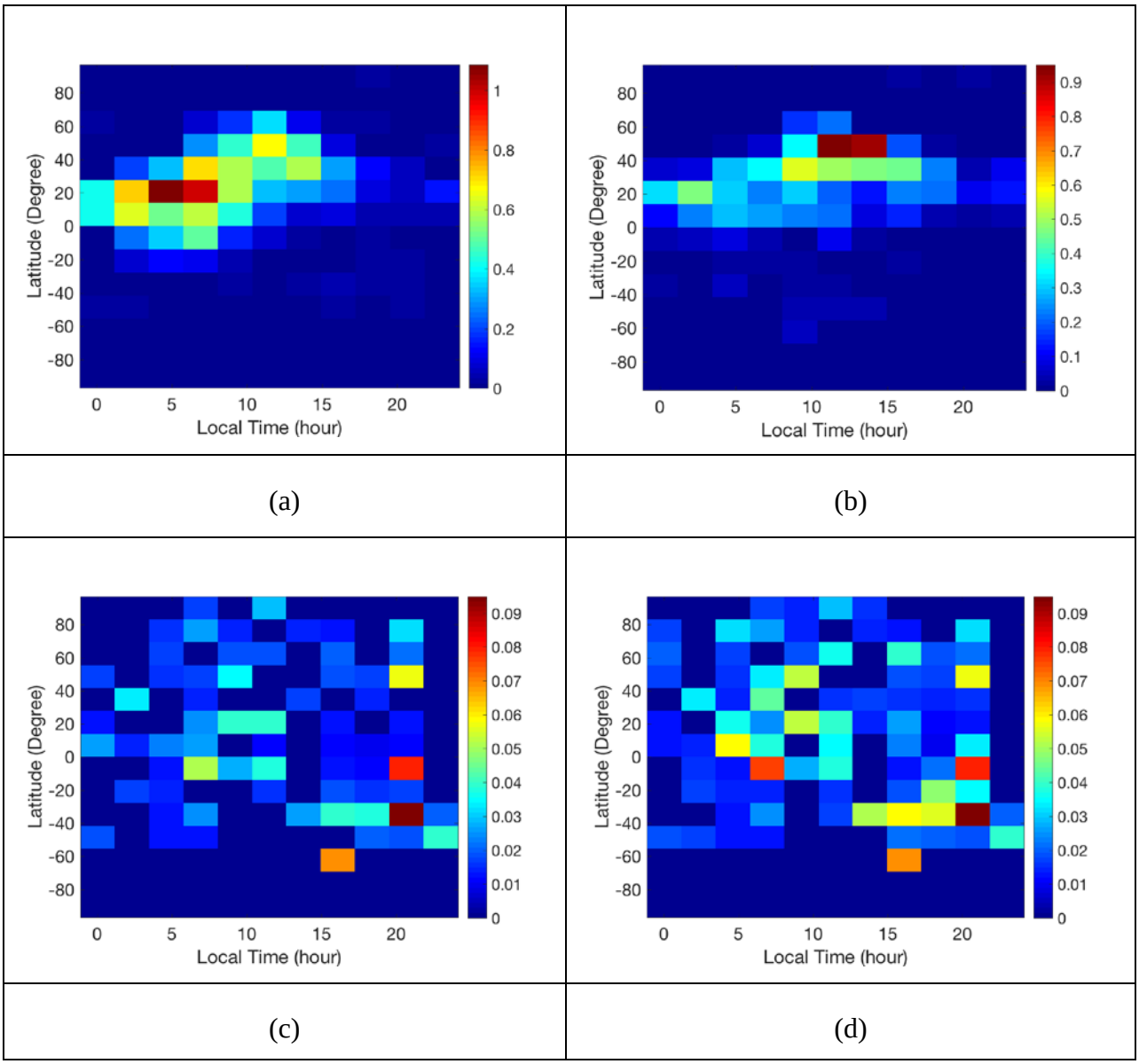

Figure 8. Normalized occurrences of events for local time and latitude (a) Coincident events; (b) NS-only events; (c) ACS-only events; (d) ACS-enhanced events.

Events of different classes show different behavior in terms of local time (LT). Coincident events are observed more often around dawn (50% between 0300 and 0900 LT), whereas the NS-only events are observed more often around noon. Conversely, ACS and ACS-enhanced events show a higher variability in local time with a stronger peak at dusk.The two-dimensional histograms in latitude versus local time normalized by the satellite coverage for the whole duration of this

study are shown in Figure 8. According to these plots, the post-midnight and early morning Coincident events are seen at latitudes between 20°S and 20°N. Coincident EE events at later local times are observed at higher latitudes. In contrast to the suprathermal electron events [*Ho et al.*, 2016], a small fraction of Coincident events is reported after 1500 LT. The ACS events are spread over all local times, but there is a larger population over evening local times and at higher latitudes in both northern and southern hemispheres.

3.3 Statistical Analyses: Energy Deposition Spectra

Here, we derive energy spectra information using an approach similar to that previously applied to obtain NS-measured energy deposition spectra (Figure 2 of *Lawrence et al.* [2015]). In order to retrieve the energy spectra associated with EE events, we need to consider the following two sets of spectra: the spectrum associated with the EE events and the background spectrum acquired during period without EE events present along the orbit. As mentioned previously, out of the 1024 energy channels of the ACS, energetic electron events are more pronounced in the low-energy channels rather than high-energy channels. Therefore, we expect the difference between the background and EE event spectra to be more pronounced in the low-energy channels. In order to derive the difference spectrum, we first scale the EE event spectrum to level the high-energy channels of both spectra, and then subtract the background spectrum from the EE event spectrum. The difference spectra can be represented by an exponential function in the form of $\boldsymbol{y = ae^{-\frac{x}{b}}}$. Parameter b of the fit provides a measure of the spectrum hardness, *i.e.* a larger b (shallower slope) indicates a more energetic EE event. An example of the background and EE spectra and the corresponding fit to the difference spectrum are shown in Figure 9.

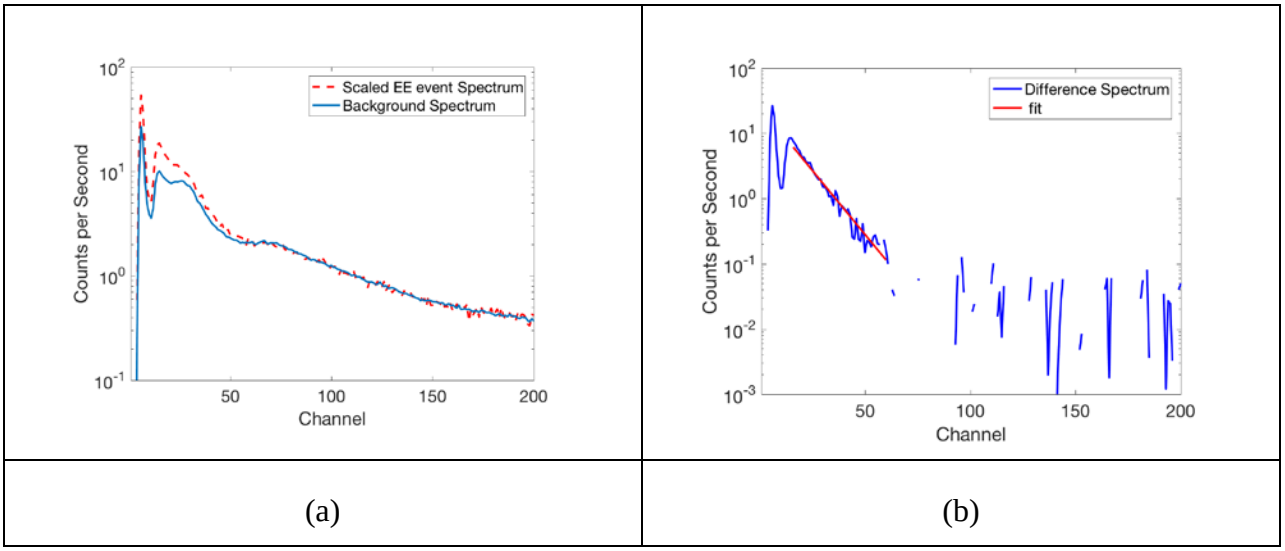

(a) (b)

Figure 9. (a) Energy deposition spectra in GRS ACS from the event on 2 February 2014. Average energy counts for the EE event and for the whole orbit without the EE event are shown in dashed red and solid blue, respectively. The trough and peak at the lowest channels (1 to 15)

are due to a lower-level discriminator cut off, and noise counts in the electronics. The statistical uncertainties on these spectra are roughly a factor of two to three larger than the point-to-point scatter in the data. (b) The difference spectrum and the corresponding exponential fit ($y = ae^{-\frac{x}{b}}$) (or linear in a logarithmic scale ($y = a_1 - \frac{x}{b}$), where $a_1 = \log(a)$) are shown in blue and red, respectively. The linear fit parameters are $a_1 = 3.26 \pm 0.27$ and $b = 11.06 \pm 0.77$.

Figure 10 shows histograms of the parameter *b* associated with the exponential fit for the Coincident and ACS-enhanced events. There are minor differences between the two histograms, such that the ACS-enhanced events may be slightly enhanced with harder spectra (e.g., slightly higher *b* values). However, based on the two-sample Kolmogorov-Smirnov goodness-of-fit hypothesis test [*Massey*, 1951], the two histograms follow a similar distribution. This result indicates that in terms of energy deposition spectra, the Coincident and ACS-enhanced events are statistically similar.

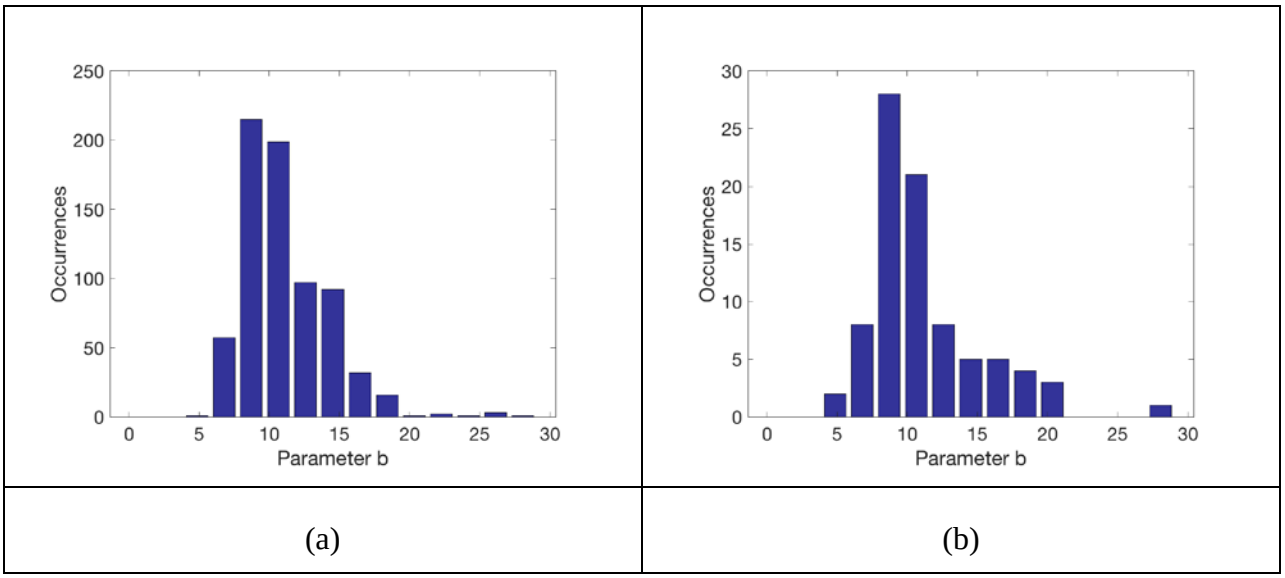

(a) (b)

Figure 10. (a) Histograms of parameter *b* of the exponential fit for Coincident events; (b) for ACS-enhanced events. This parameter is a proxy for the hardness of spectrum, where larger *b* indicates a harder spectrum. Based on the two-sample Kolmogorov-Smirnov goodness-of-fit hypothesis test, the two histograms follow a statistically similar distribution.

3.4 Statistical Analyses: Location and Orientation with Respect to Mercury's Magnetic Field

Because physical drivers for the injection and transport of energetic electrons are related to Mercury's dynamic magnetosphere, studying the behavior of EE events with respect to magnetic field parameters is necessary to gain an understanding of Mercury's magnetosphere. The multi-

instrument analysis of this work can provide characterization of possible directional anisotropies of the EE events.

The magnetic field parameters considered in this study include magnetic field location, expressed as invariant latitude and magnetic local time (MLT), and orientation of the sensors and spacecraft with respect to Mercury's magnetic field. MLT is expressed in the Mercury solar magnetospheric (MSM) coordinates, which is based on the Mercury solar orbital (MSO) coordinate system, except for a dipole offset of 479 km in the +*z* MSO direction [*Korth et al.*, 2015]. The invariant latitude and MLT are derived from the KT14 magnetic field model [*Korth et al.*, 2015]. Note that because Mercury does not have a dipole tilt, MLT is the same as LT.

Figure 11 summarizes the locations of EE events in terms of invariant latitude and MLT for Coincident and ACS-enhanced events. NS-only and ACS-only events, not plotted here, show similar characteristics to Coincident and ACS-enhanced, respectively. Note that these parameters are not available for events that occur outside the model Mercury's magnetic field. These events amount to 38% of the total ACS-enhanced events. The histograms are normalized by the satellite coverage of the invariant latitude-MLT space of the spacecraft for the entire period of study (with altitude <= 4000 km). The white area between ±20 degrees invariant latitude indicates that the spacecraft never pass through this region. This is because magnetic field lines near the equator close at altitudes which are lower than spacecraft periapsis.

Similar to geographical distributions, EE-event occurrences within Mercury's magnetic field show different characteristics for Coincident events compared to ACS-enhanced events. In general, the locations of Coincident events are similar to the locations for NS-measured events for 8-hour orbit data [*Lawrence et al.*, 2015]. Coincident events dominantly occur in the northern hemisphere, while a significant fraction of ACS-enhanced events occur in both hemispheres. In regards to MLT, Coincident events are concentrated in pre-noon MLTs whereas ACS-enhanced events are more uniformly distributed for all MLT values.

The white lines in Figure 11 indicate the modeled boundary between open and closed magnetic field lines [*Korth et al.*, 2014].The majority (97%) of Coincident events occurred within the region of closed magnetic field lines, similar to the results of *Lawrence et al*. [2015]. Conversely, 31% of total ACS-enhanced events occurred within the open magnetic field-line region (Note that 51% of events within model magnetic field (%62 of total ACS events) occur on open field lines). These events plus the ACS-enhanced events that were located outside the model magnetosphere have moderate to high spectral indices (exponential fit parameter *b* is between 10 and 20) [*Korth et al*., 2015, *Ho et al*., 2016].

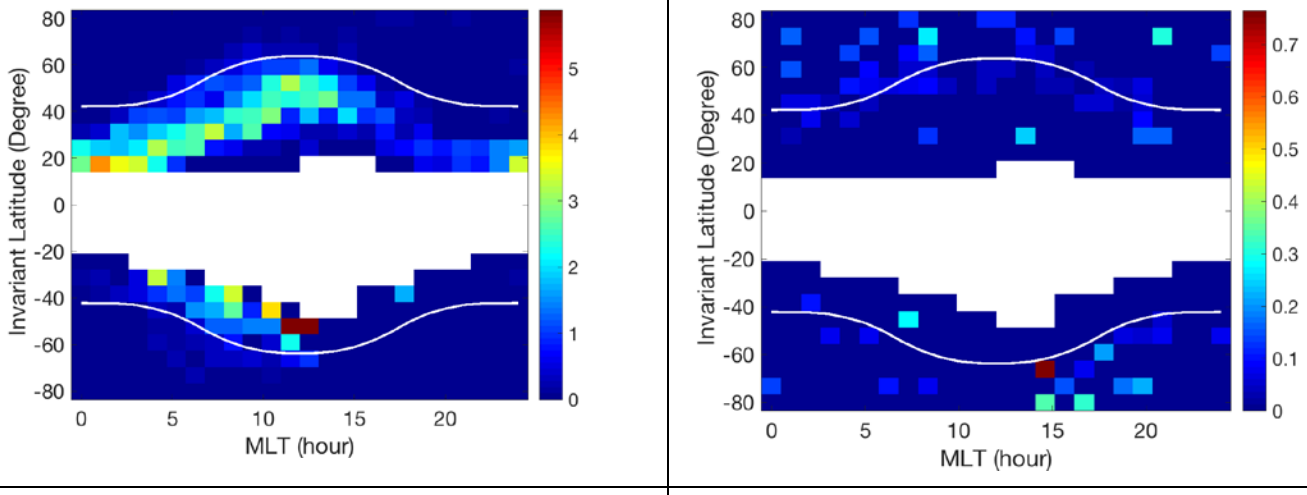

Figure 11. Two-dimensional normalized histograms of EE events for invariant latitude versus MLT. (a) Coincident events. (b) ACS-enhanced events. The normalization is performed based on the MLT - invariant latitude space covered by the spacecraft for the entire time between 1 March 2013 and 30 April 2015, when the spacecraft altitude was 4000 km or less from Mercury surface. The modeled boundary between the open and closed field lines is shown by the white lines. The white area between ±20 degrees invariant latitude indicates that the spacecraft was never located in these areas.

To see if these events indicate any directional anisotropies with respect to the magnetic field, we plot the angle between the measured magnetic field and *x*, *y*, and *z* axes of the spacecraft in the MSO coordinate system in Figures 12–14, respectively. The spacecraft coordinates are shown in Figure 1 of *Feldman et al.*, [2010] as well as Figure 15 (a), and are oriented such that the *x*-axis is parallel to solar panel axis, the *y*-axis is parallel to the magnetometer boom, and the *z*-axis points in the direction of the adapter ring. We choose the actual magnetic field instead of modeled magnetic field to be able to include the 38% of the ACS-enhanced events that occur outside of the model magnetosphere and to have better statistics. Both bursty and smooth Coincident event distributions show distinct peaks when the angle between the magnetic field vector and the *x*-axis of the spacecraft is 180° (Figure 12(a)). Smooth NS-only events follow the same characteristics, but the bursty NS-only events show a more uniform distribution for all angles. This means that the Coincident and NS-only events are dominantly detected when the magnetic field vector and the *x*-axis of the spacecraft are quasi-parallel. In contrast, ACS-only and ACS-enhanced events show a more uniform distribution for all angles, although there is a slight enhancement around 70° for bursty ACS-only events.

Histograms of the angles between the measured magnetic field vector and the *y*- and *z*-axes of the spacecraft for Coincident events (both smooth and bursty) show relatively narrow distributions around 90° (Figures 13 and 14). NS-only events show a wider distribution but are still peaked around 90°. This means that for the majority of the EE events the magnetic field vector was nearly perpendicular to the *y*- and *z*-axes of the spacecraft. In contrast, ACS-only and ACS-enhanced events have a wider dynamic range from 50° to 110° with a peak around 80°. We should note that the magnetic field related parameters utilized for these histograms are based on the magnetic field at the peak of the event. For some events, there is a considerable variation in magnetic field for the duration of the events, which is not reflected in these histograms.

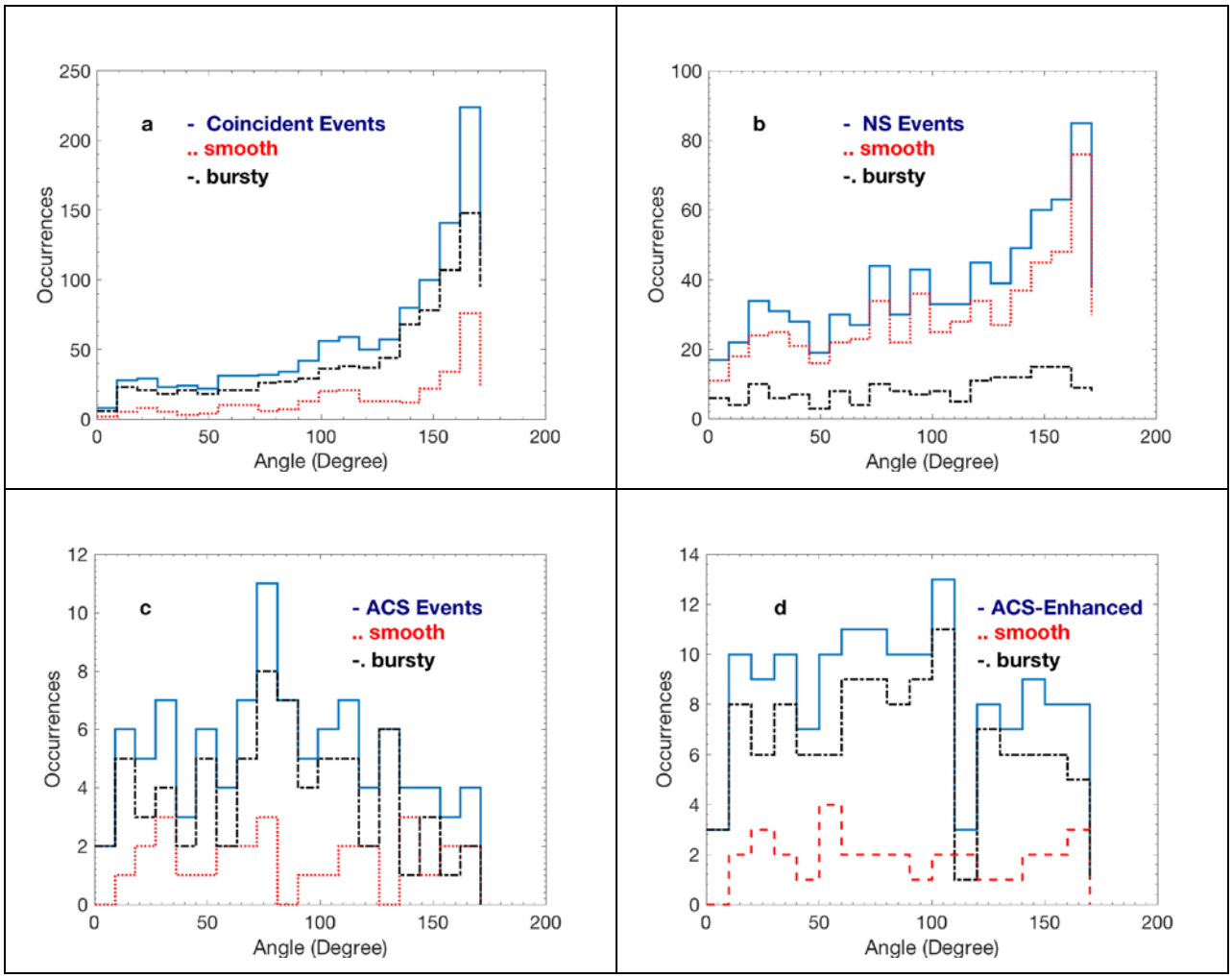

Figure 12. Histograms of the angle between the measured magnetic field vector and *x*-axis of the spacecraft in MSO coordinates. (a) Coincident events; (b) NS-only events; (c) ACS-only events; (d) ACS-enhanced events.

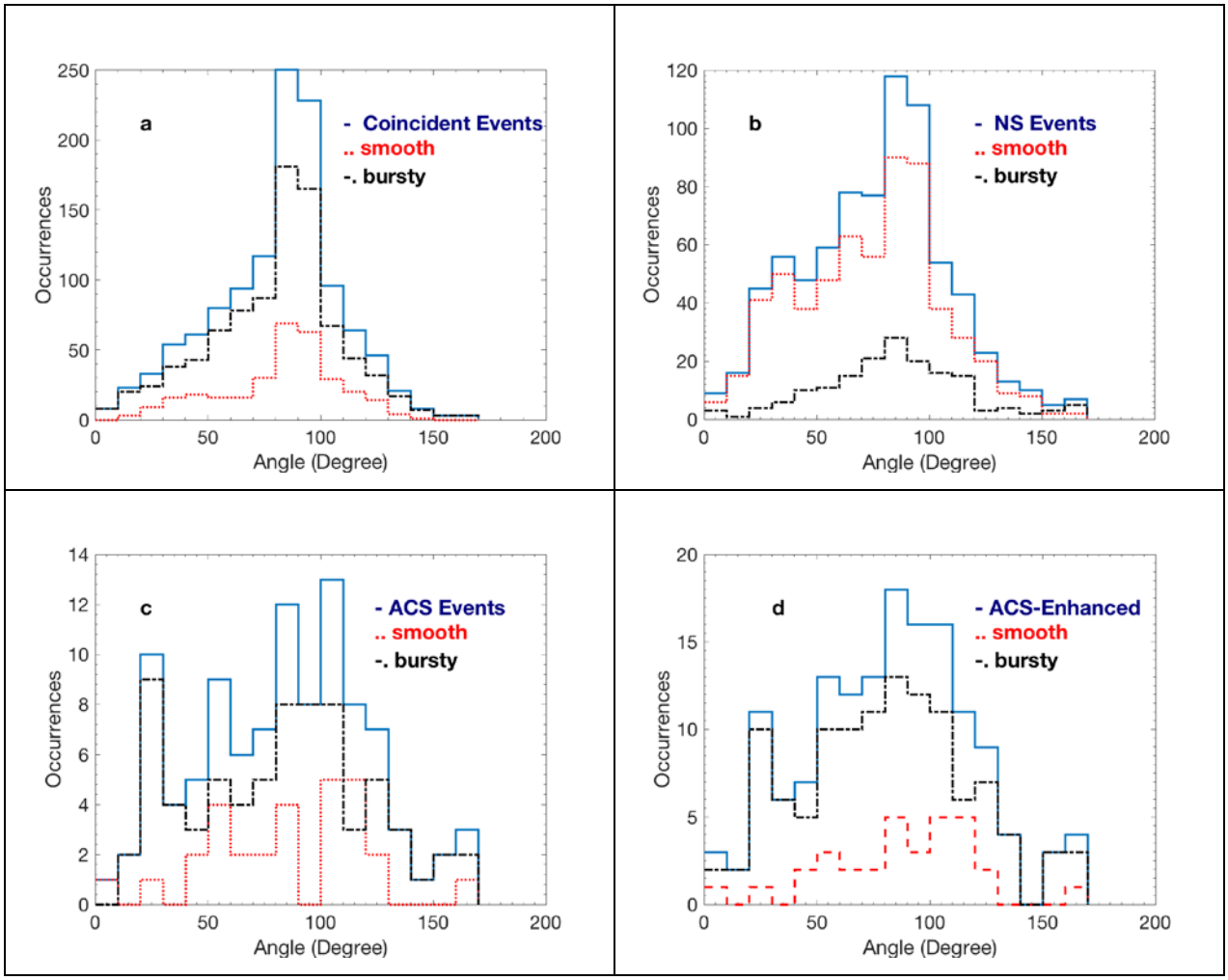

Figure 13. Histograms of the angle between the measured magnetic field vector and *y*-axis of the spacecraft in MSO coordinates. (a) Coincident events; (b) NS-only events; (c) ACS-only events; (d) ACS-enhanced events.

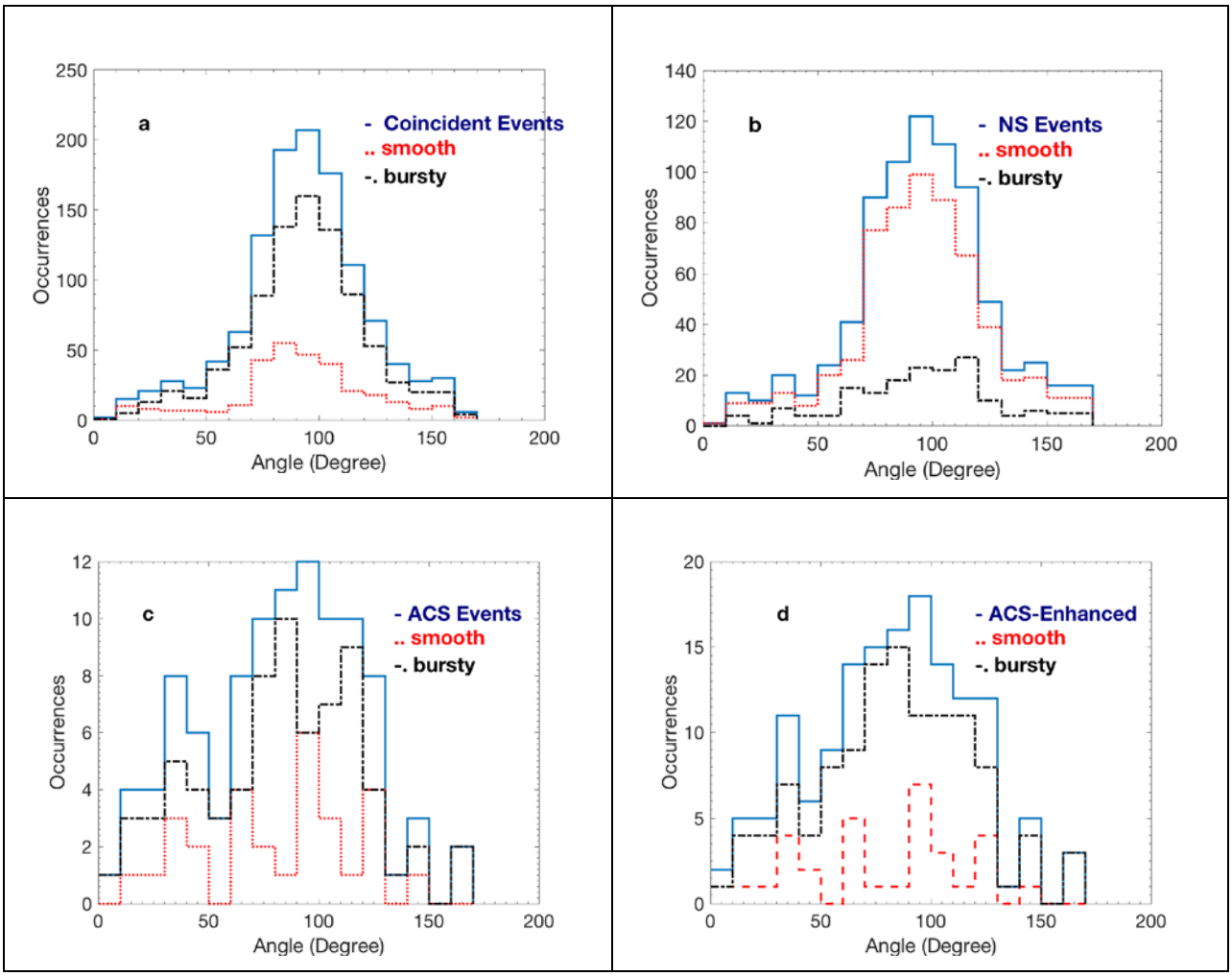

Figure 14. Histograms of the angle between the measured magnetic field vector and *z*-axis of the spacecraft in MSO coordinates. (a) Coincident events; (b) NS-only events; (c) ACS-only events; (d) ACS-enhanced events.

4. Discussion

A majority of the detected EE events are seen in both the NS and ACS sensors, which we have called Coincident events. The intrinsic characteristics, distribution of geographical locations, and distribution of magnetic field locations and orientations for most of the Coincident events are similar to the NS-measured events described by *Lawrence et al*. [2015]. Based on the measured parameters described Sections 3.1, 3.2, and 3.4, as well as the SNR plot of Figure 2(a), the NS-only events are likely a subset of the Coincident events that were only detected in the NS due to its higher sensitivity. In contrast, ACS-only events have similar characteristics to ACS-enhanced

events, with similar distributions of event duration, event size, and altitude; latitude and local time, as well as magnetic field orientation with respect to the spacecraft. In addition, the measured parameters for ACS-only and ACS-enhanced events are distinctly different than those for the Coincident and NS-only events.

Based on the observed similarity between Coincident and NS-only events, and the observed similarity between ACS-only and ACS-enhanced events, we are led to conclude that for all the events measured by the NS and ACS, there are only two types of dominant classes. Because the Coincident and NS-only events comprise the majority of the events, we define these as "Standard events". In contrast, ACS-enhanced events, which include ACS-only events, are already defined as events that lie above the one-to-one line in Figure 2(b).

Parameter	**Standard Events**	**ACS-enhanced Events**
Number	1914	147
Percentage of total	93%	7%
Correlation of NS and ACS SNR	Most within one-standard deviation of one-to-one line.	ACS SNR is enhanced by factors of 10 to ~100.
Bursty versus smooth	Mix of both.	Most are bursty.
Event SNR distribution	Power law distribution Mean power-law index = -0.53	Power law distribution Mean power-law index = -0.78
Event duration	Event lengths up to 20 min; mean lengths >5 min.	Most shorter than 5 min; mean lengths a few min.
Latitude/altitude	Peaked at mid-latitudes (30°N to 40°N). Altitudes generally <1000 km.	Wide range of latitudes from 50°S to 80°N. Wide range of altitudes from few hundred km to ~4000 km.
Local time	Distribution peaked in the range of dawn to noon.	Wide distribution with local peaks around dawn and dusk.
Energy spectra	Two classes are similar, but with ACS-enhanced possibly having slight enhancement of harder spectra.	
Distribution within magnetic field	Almost all events occur on closed field lines.	38% of events occur outside model magnetic field. Equal number of events within model magnetic field occur on open and close field lines.
Magnetic field orientation	Distribution of magnetic field to s/c coordinate system is peaked in the parallel direction to s/c *x*-axis and perpendicular direction to s/c *y*-and *z*- axes.	Distribution of magnetic field to s/c coordinate system is mostly uniform with respect to s/c *x*-axis and broadly perpendicular to s/c *y*- and *z*- axes.

	Consistent with a 90-degree pitch angle distribution.	More consistent with a beam-like distribution.

Table 2. Summary of event characteristics for Standard and ACS-enhanced events.

Standard events comprise the large majority of all EE events (93%). Standard events are similar in character to the typical NS-detected EE events described by *Lawrence et al.* [2015]. Specifically, Standard events have a mix of bursty and smooth types and exhibit a range of durations and SNR magnitudes. We note that the SNR histogram of NS-only events, a subclass of Standard events, has a different and shallower slope than that of other Standard events (e.g., Figure 3). However, this is likely due to the selection effects of the NS-only events having a lower SNR because they are detected by the more sensitive NS. In terms of geographic and magnetic field location, Standard events are also similar to the prior NS-detected events in *Lawrence et al.* [2015], because they are generally seen at mid-latitudes and lower altitudes on closed field lines in the dawn-to-noon local time sector. Finally, the orientation of the spacecraft with respect to the magnetic field is parallel to the spacecraft *x*-axis and perpendicular to the spacecraft *y*- and *z*-axes.

In contrast, ACS-enhanced events represent a new class of event, the identification of which has been enabled by the comparison of NS and ACS detections. While ACS-enhanced events tend to have a similar shaped SNR power-law distribution as Standard events (albeit with fewer occurrences because ACS-enhanced events are less than 10% of all detected EE events), all other characteristics of ACS-enhanced events are different from Standard events. They generally have shorter durations than Standard events, they are mostly bursty, and they are widely distributed in latitude, altitude, local time, and within (and even outside) Mercury's magnetosphere. Importantly, their SNR magnitude in the ACS is a factor of 10 to 100 larger than observed in the NS. Finally, the orientation of the spacecraft with respect to the magnetic field for ACS-enhanced detections is distinctly different for Standard events, such that there is a wider and more uniform distribution of angles than for Standard events. Table 2 provides a summary of the various event parameters and characteristics as delineated by these two final defined event classes.

Based on this information, we conclude that one primary difference between Standard and ACS-enhanced events is that Standard events primarily follow a distribution that peaks around pitch angle ~ 90°) with respect to Mercury's magnetic field, whereas ACS-enhanced events are primarily beam-like. This conclusion is based on four observations. First, Standard events have the same SNR magnitude in both the NS and ACS to within a few percent (Figure 2). Second, the distribution of magnetic field orientations with respect to the spacecraft coordinate frame is peaked when the magnetic field is parallel to the *x*-axis (and therefore necessarily also peaked when the magnetic field is perpendicular to the spacecraft *y*- and *z*-axes). Third, we note that the detection responses of the NS and ACS are likely quite different due to their locations on the MESSENGER spacecraft. Referring to Figure 1 of *Feldman et al.* [2010] and Figure 15, note that the NS is located on the back of the spacecraft behind the sunshade, and it is therefore

completely blocked by the spacecraft from electrons moving in directions between the -*y*-axis direction to the +y-axis direction. In addition, the NS is partially blocked by the phased array antenna for angles ranging between the +*y*-axis and the +*x*-axis direction. In contrast, the ACS is open to more angles as it is located at the bottom (instrument deck) of the spacecraft. Specifically, it is only blocked by the adapter ring, which has significantly less material than the full spacecraft that blocks half of the NS field-of-view. These angles of blockage range roughly from the ϕ = ~315° to 360° and from 0° to ϕ=~45°. Energetic electrons coming from the –*y*-axis to the +*y*-axis direction into the ACS do have to travel through the sunshade. However, the sunshade is a thin fabric, so it likely provides little attenuation to the energetic electrons. Therefore, both the NS and GRS have a maximum response to electrons moving either in the direction of the spacecraft –*x*-axis (or ϕ ~ 180°), in the +*z*-axis to –*z*-axis direction, or in the +*y*-axis to –*y*-axis direction. Fourth, Standard events are mostly observed in the post-midnight (dawn) sector at mid-latitudes, where the XRS also observed a high frequency of suprathermal electron events [*Ho et al.*, 2016]. Compared to NS and GRS, XRS has a much more limited field of view (FOV), able to detect predominately electrons moving from the +*z*-axis to –*z*-axis, which is perpendicular to the magnetic field (parallel with the *x*-axis) during these events. Therefore, XRS could only observe the electrons that are gyrating about the field line (perpendicular to the magnetic field) in the *y*-*z* plane in the spacecraft frame. Thus, we conclude that the majority of the Standard events are gyrating about the field

The directionality analysis of this work supports the updated injection model described by *Dewey et al.* [2017] and observations by *Lindsay et al.* [2016]. *Dewey et al.* [2017] suggests electrons that drift eastward about the planet following magnetotail energization and injection participate in Shabansky-like orbits, in which the guiding center migrates to higher latitudes in the northern hemisphere due to compression of Mercury's dayside magnetosphere. Only gyrating electrons participate in the Shabansky-like orbits (field-aligned electrons are not able to execute these orbits). The observation that the majority of electron events about Mercury are comprised of 90-degree pitch angle distributions is therefore consistent with Shabansky-like orbits and further supports the model that these electron events may have been energized in Mercury's magnetotail and subsequently injected close to the planet.

In contrast to Standard events, ACS-enhanced events have a larger SNR magnitude in the ACS than in the NS and occur with more variable spacecraft orientation with respect to the local magnetic field. While the more variable spacecraft orientation may suggest that ACS-enhanced events have a more isotropic distribution than Standard events, such a distribution is not consistent with the large SNR difference between events in the ACS and NS. Instead, ACS-enhanced events could resemble beam-like distributions. If a beam, for example, was traveling from +*x* to –*x* or from –*y* to +*y* in the spacecraft frame, the NS FOV would be blocked by varying amounts of spacecraft materials while the ACS FOV would more clearly see the electrons and therefore detect a larger signal. Such beam-like distributions of energetic electrons may be produced by mechanisms including magnetic reconnection (e.g., [*Drake et al.*, 2005]) and foreshock interaction (e.g., [*Fitzenreiter*, 1995]). Most ACS-enhanced events are observed near

the open/closed field line boundary (see Figure 11) or outside the magnetosphere, consistent with reconnection and foreshock acceleration, respectively. However, the local time distribution of this class of events is not fully consistent with these acceleration mechanisms. ACS-enhanced events are most frequently observed near the terminators (see Figure 7), while magnetic reconnection is expected to occur closer to the meridional plane and the electron foreshock is expected to form at prenoon local times. While asymmetries in Mercury's system might produce beam-like distributions closer to the observed ACS-enhanced event locations, e.g., magnetotail reconnection has a cross-tail bias favoring the post-midnight region [*Sun et al*., 2016] and could produce electron beams at local times ~2-4. Further investigation is required to understand the acceleration mechanism(s) of this class of events and will be the focus of our future work.

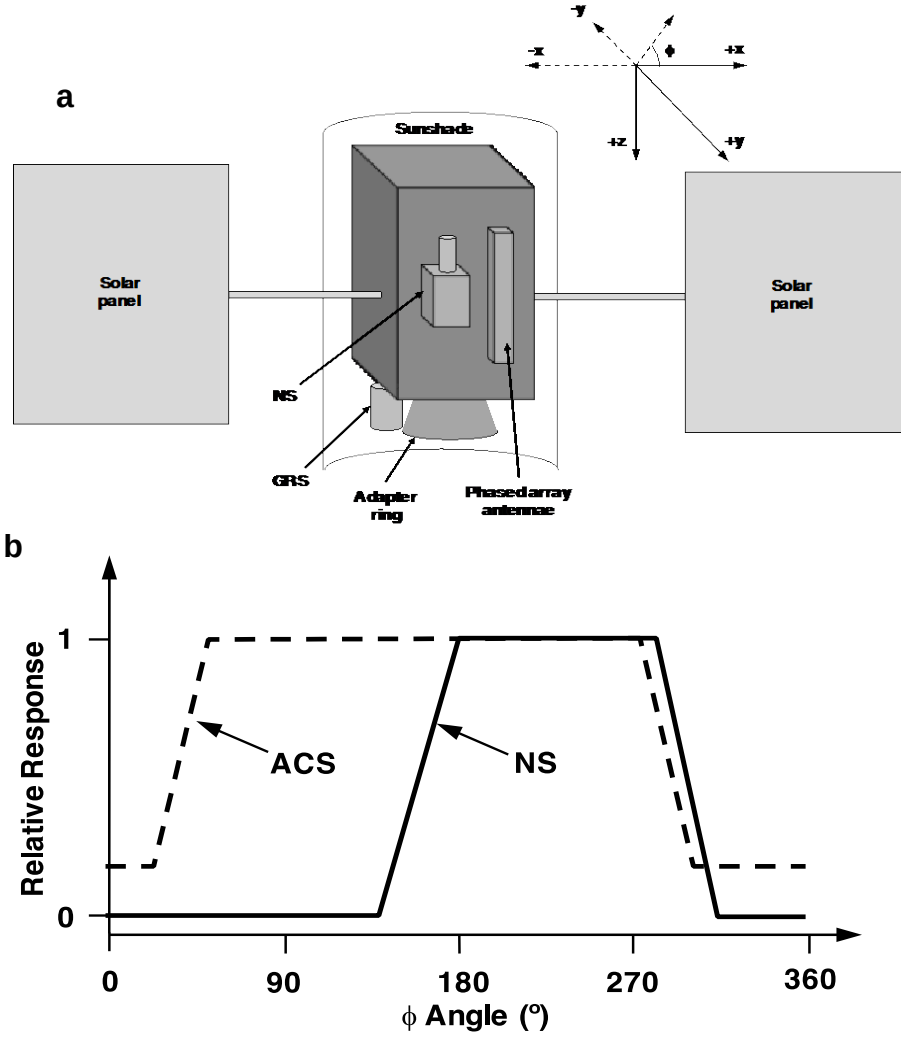

Figure 15. (a) Schematic view of the MESSENGER spacecraft where specific components relevant to this study are labeled including the NS, GRS, adapter ring, and phased array antennae. The spacecraft coordinate system is shown in the upper right, where the angle ϕ is given in the *x*-*y* plane. $\phi = 90°$ represents electrons traveling in the –*y*-axis to +*y*-axis direction. (b) Schematic response of the NS (solid) and ACS (dashed) as a function of ϕ angle.

In order to gain better understanding of these two classes and their angular distributions (and ultimately their acceleration mechanisms), a number of future tasks should be carried out. First, a quantitative angular response of the NS and ACS for the detection of energetic electrons needs to be calculated. This can be carried out using a particle transport code such as MCNPX [*Pelowitz*, 2005] or GEANT [*Agostinelli et al.*, 2003]. For such response calculations, careful attention is needed to understand properly the role that sensor and spacecraft housing material has in creating and transporting the bremsstrahlung radiation that is ultimately detected in the NS and ACS sensors. We note that prior particle transport calculations of the NS and GRS/ACS have already been carried out for neutrons and gamma rays where the housing and spacecraft materials have been taken into account [*Peplowski et al*., 2012; *Lawrence et al*., 2013, 2014, 2015]. Second, to understand better the detailed characteristics of Standard versus ACS-enhanced events, case studies and/or superposed epoch analyses [e.g., like *Dewey et al*., 2017] of ACS-enhanced events can be carried out to determine the if the ratio of ACS to NS SNR varies with the local magnetic-field direction. If such a correlation is found, this would provide supporting evidence that ACS-enhanced events have a beam-like population.

5. Summary

We carried out the first comprehensive analysis of EE events at Mercury as measured with the MESSENGER GRS ACS. The EE events detected with the ACS were then compared to EE-event detections with MESSENGER's NS. This analysis was conducted using over two year's worth of data in Mercury orbit from early 2013 to the end of the MESSENGER mission in April 2015. With this study, we have established a number of conclusions regarding EE events around Mercury.

1. When using the combined ACS and NS datasets, there are two classes of EE events. The first class, Standard events, comprise over 90% of all events, and are similar to the EE events characterized by the NS and described by *Lawrence et al*. [2015].

2. This study has identified a new class of EE events that are called ACS-enhanced events because their signal size is enhanced by a factor of 10 to 100 over that seen in the NS. In contrast, the signal size of Standard events is roughly the same in both the ACS and NS. ACS-enhanced events comprise approximately 7% of all detected events.

3. The characteristics of Standard and ACS-enhanced events differ in many aspects. Most importantly, the characteristics of Standard events are consistent with energetic electrons

that are gyrating about the magnetic field, whereas the characteristics of ACS-enhanced events are consistent with electrons that follow a beam-like distribution. The ability to carry out this initial assessment of the EE directionality is enabled by the different viewing geometries of the ACS and NS.

4. In addition to EE directionality, ACS-enhanced events differ from Standard events in that they tend to be more bursty, occur over a wider range of latitudes, altitudes, and local times, and are not confined to Mercury's magnetosphere. All of these characteristics suggest that ACS-enhanced events are generated by a different type of acceleration process than Standard events.

Understanding the character of these two different classes requires additional work both in refining sensor response models and carrying out detailed studies of individual events and groups of events.

Acknowledgments

This work is supported by NASA grants from the MESSENGER Participating Scientist and Discovery Data Analysis programs (grant numbers NNX08AN30G and NNX16AI98G) to the Johns Hopkins University Applied Physics Laboratory. All original data reported in this paper are archived by the NASA Planetary Data System (http://pds-geosciences/wustl.edu/ missions/messenger/index.htm).

References

Agostinelli, S., et al. (2003), GEANT4—A simulation toolkit, *Nucl. Instrum. Methods Phys. Res.*, Sect. A, 506, 250–303, doi:10.1016/S0168-9002 (03)01368-8.

Alexeev, I. I. , E. S. Belenkaya, J. A. Slavin, Haje Korth, B. J. Anderson, D. N. Baker, S. A. Boardsen, C. L. Johnson, M. E. Purucker (2010), Mercury's magnetospheric magnetic field after the first two MESSENGER flybys, *Icarus*, 209, 23–39, doi:10.1016/ j.icarus.2010.01.024.

Armstrong, T. P., S. M. Krimigis, and L. J. Lanzerotti (1975), A reinterpretation of the reported energetic particle fluxes in the vicinity of Mercury, *J. Geophys.* Res., 80, 4015–4017.

Armstrong, T. P., L. J. Lanzerotti, and S. M. Krimigis (1979), Comment on "Electron calibration of instrumentation for low-energy high-intensity particle measurements at Mercury" by Christon, Daly, Eraker, Perkins, Simpson, and Tuzzolino, J. Geophys. Res., 84, 4468–4469.

Baker, D. N., J. A. Simpson, and J. H. Eraker (1986), A model of impulsive acceleration and transport of energetic particles in Mercury's magnetosphere, *J. Geophys. Res.*, 91, 8742–8748, doi:10.1029/ JA091iA08p08742.

Baker, D. N., R. C. Anderson, R. D. Zwickl, and J. A. Slavin, Average Caan, M. N., R. L. McPherron, and C. T. Russell (1987), The statistical magnetic plasma and magnetic field variations in the distant magnetotail associated with near-Earth substorm effects, *J. Geophys. Res.*, 92, 71-82.

Baker, D. N., T. I. Pulkkinen, V. Angelopoulos, W. Baumjohann, and R. L. McPherron (1996), Neutral line model of substorms: Past results and present view, *J. Geophys. Res.*, 101(A6), 12975–13010, doi:10.1029/95JA03753.

Baker, D. N., R. M. Dewey, D. J. Lawrence, J. O. Goldsten, P. N. Peplowski, H. Korth, J. A. Slavin, S. M. Krimigis, B. J. Anderson, G. C. Ho, et al. (2016), Intense energetic electron flux enhancements in Mercury's magnetosphere: An integrated view with high-resolution observations from MESSENGER, *J. Geophys. Res. Space Physics*, 121, 2171–2184, doi:10.1002/2015JA021778.

Dewey, R. M., J. A. Slavin, J. M. Raines, D. N. Baker, D. J. Lawrence (2017), Energetic Electron Acceleration and Injection During Dipolarization Events in Mercury's Magnetotail, *J. Geophys. Res. Space Physics*, 122, 12,170 –12,188, doi:10.1002/2017JA024617.

Drake, J. F., et al. (2005), Production of Energetic Electrons during Magnetic Reconnection, *Phys. Rev. Lett.*, **94**, doi:10.1103/PhysRevLett.94.095001.

Evans, L. G., P. N. Peplowski , E. A. Rhodes , J. O. Goldsten , R. D. Starr , S. C. Solomon (2017), The MESSENGER Gamma-Ray Spectrometer: Calibration and Operations, *Icarus*, 288, 186 – 200, doi:10.1016/j.icarus.2017.01.022.

Feldman, William C., D. J. Lawrence, J. O. Goldsten, R. E. Gold, D. N. Baker, D. K. Haggerty, G. C. Ho, S. Krucker, R. P. Lin, R. A. Mewaldt, R. J. Murphy, L. R. Nittler, E. A. Rhodes, J. A. Slavin, S. C. Solomon, R. D. Starr, F. Vilas, and A. Vourlidas (2010), Evidence for Extended Acceleration of Solar-Flare Ions from 1–8-MeV Solar Neutrons Detected with the MESSENGER Neutron Spectrometer, *J. Geophys. Res.*, 115, A01102, 10.1029/2009JA014535.

Fitzenreiter, R. J. (1995), The electron foreshock, *Adv. Space Res.*, 15, 9–27, doi:10.1016/0273-1177(94)00081-B.

Gershman, D. J., et al. (2015), MESSENGER observations of solar energetic electrons within Mercury's magnetosphere, *J. Geophys. Res. Space Physics*, 120, 8559–8571, doi:10.1002/2015JA021610.

Goldsten, J. O., et al. (2007), The MESSENGER Gamma-Ray and Neutron Spectrometer, *Space Sci. Rev.*, 131, 339–391, doi:10.1007/s11214-007-9262-7.

Ho, G. C., et al. (2011a), MESSENGER observations of transient bursts of energetic electrons in Mercury's magnetosphere, *Science*, 333, 1865–1868, doi:10.1126/science.1211141.

Ho, G. C., R. D. Starr, R. E. Gold, S. M. Krimigis, J. A. Slavin, D. N. Baker, B. J. Anderson, R. L. McNutt Jr., L. R. Nittler, and S. C. Solomon (2011b), Observations of suprathermal electrons in Mercury's magnetosphere during the three MESSENGER flybys, *Planet. Space Sci.*, 59, 2016–2025.

Ho, G. C., S. M. Krimigis, R. E. Gold, D. N. Baker, B. J. Anderson, H. Korth, J. A. Slavin, R. L. McNutt Jr., R. M. Winslow, and S. C. Solomon (2012), Spatial distribution and spectral characteristics of energetic electrons in Mercury's magnetosphere, *J. Geophys. Res.*, 117, A00M04, doi:10.1029/2012JA017983.

Ho, G. C., R. D. Starr, S. M. Krimigis, J. D. Vandegriff, D. N. Baker, R. E. Gold, B. J. Anderson, H. Korth, D. Schriver, R. L. Jr. McNutt, et al. (2016), MESSENGER observations of suprathermal electrons in Mercury's magnetosphere, *Geophys. Res. Lett.*, 43, 550–555, doi:10.1002/2015GL066850.

Johnson, C. L., et al. (2012), MESSENGER observations of Mercury's magnetic field structure, *J. Geophys. Res.*, 117, E00l14, doi:10.1029/2012JE004217.

Korth, H., B. J. Anderson, D. J. Gershman, J. M. Raines, J. A. Slavin, T. H. Zurbuchen, S. C. Solomon, and R. L. McNutt, Jr. (2014), Plasma distribution in Mercury's magnetosphere derived from MESSENGER Magnetometer and Fast Imaging Plasma Spectrometer observations, *J. Geophys. Res. Space Physics*, *119*, 2917−2932, doi: 10.1002/2013JA019567.

Korth, H., N. A. Tsyganenko, C. L. Johnson, L. C. Philpott, B. J. Anderson, M. M. Al Asad, S. C. Solomon, and R. L. McNutt Jr. (2015), Modular model for Mercury's magnetospheric magnetic field confined within the average observed magnetopause, *J. Geophys. Res. Space Physics*, 120, 4503–4518, doi:10.1002/ 2015JA021022.

Lawrence, David J. et al., (2013), Evidence for Water Ice Near Mercury's North Pole from MESSENGER Neutron Spectrometer Measurements, *Science*, 339, 292–296, doi:10.1126/science.1229953.

Lawrence, David J. et al., (2014), William C. Feldman, John O. Goldsten, Patrick N. Peplowski, Douglas J. Rodgers, and Sean C. Solomon, Detection of 0.5 – 8 MeV Neutrons Near Mercury: Evidence for a Solar Origin, *J. Geophys. Res. Space Physics*, 119, 5, 5150 – 5171, 10.1002/2013JA019037.

Lawrence, David J., et al., (2015), Comprehensive survey of energetic electron events within Mercury's magnetosphere using data from the MESSENGER Neutron and Gamma-Ray Spectrometers, *J. Geophys. Res. Space Physics*, 10.1002/2014JA020792.

Lawrence, D. J., P. N. Peplowski,W. C. Feldman, N. A. Schwadron, and H. E. Spence (2016), Galactic cosmic ray variations in the inner heliosphere from solar distances less than 0.5 AU: Measurements from the MESSENGER Neutron Spectrometer, *J. Geophys. Res. Space Physics*, 121, 7398–7406, doi:10.1002/2016JA022962.

Lindsay, S.T., James, M.K., Emma Bunce, S.M. Imber, H. Korth, A. Martindale, and T. Yeoman (2016). MESSENGER X-ray observations of magnetosphere-surface interaction on the nightside of Mercury. Planetary and Space Science. . 10.1016/j.pss.2016.03.005.

Massey, F. J. (1951), The Kolmogorov-Smirnov Test for Goodness of Fit, *Journal of the American Statistical Association*. Vol. 46, No. 253, pp. 68–78.

Pelowitz, D.B., 2005. MCNPX User's Manual, Version 2.5.0., Los Alamos National Laboratory report LA-CP-05-0369, Los Alamos, NM.

Peplowski, P. N., et al. (2012), Variations in the abundances of potassium and thorium on the surface of Mercury: Results from the MESSENGER Gamma-Ray Spectrometer, *J. Geophys. Res.*, 117, E00L04, doi:10.1029/2012JE004141.

Peplowski P.N., D.J. Lawrence, W.C. Feldman, J.O. Goldsten, D. Bazell, L.G. Evans, J.W. Head, L.R. Nittler, S.C. Solomon, S.Z. Weider (2015), Geochemical terranes of Mercury's northern hemisphere as revealed by MESSENGER neutron measurements, *Icarus*, 253, 346–363.

Russell, C. T., Baker, D. N. and Slavin, J. A. (1988) The magnetosphere of Mercury. In Mercury, ed. C. Chapman, pp. 5 14-56 1. University of Arizona Press, Tucson.

Simpson, J. A., Eraker, J. H. Lamport, J. E., and W. P. H. (1974), Electrons and protons accelerated in mercury's magnetic field, *Science*, 185, 160–166, doi:10.1126/ science.185.4146.160.

Slavin, J. A., et al. (2010), MESSENGER observations of extreme loading and unloading of Mercury's magnetic tail, *Science*, 329, 665–668, doi:10.1126/science.1188067.

Starr, R. D., D. Schriver, L. R. Nittler, S. Z. Weider, P. K. Byrne, G. C. Ho, E. A. Rhodes, C. E. Schlemm II, S. C. Solomon, and P. M. Trávníček (2012), MESSENGER detection of electron-induced X-ray fluorescence from Mercury's surface, *J. Geophys. Res.*, 117, E00L02, doi:10.1029/2012JE004118.

Sun, W. J., et al. (2016), Spatial distribution of Mercury's flux ropes and reconnection fronts: MESSENGER observations, *J. Geophys. Res. Space Physics*, **121**, doi:10.1002/2016JA022787.

Walsh B. M., A. S. Ryou, D. G. Sibeck, and I. I. Alexeev (2013), Energetic particle dynamics in Mercury's magnetosphere, J. Geophys. Res. Space Physics, 118, 1992-1999, doi:10.1002/jgra.50266.

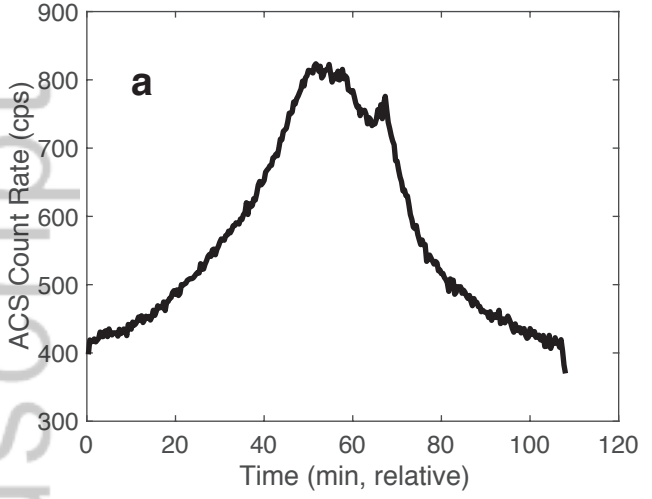

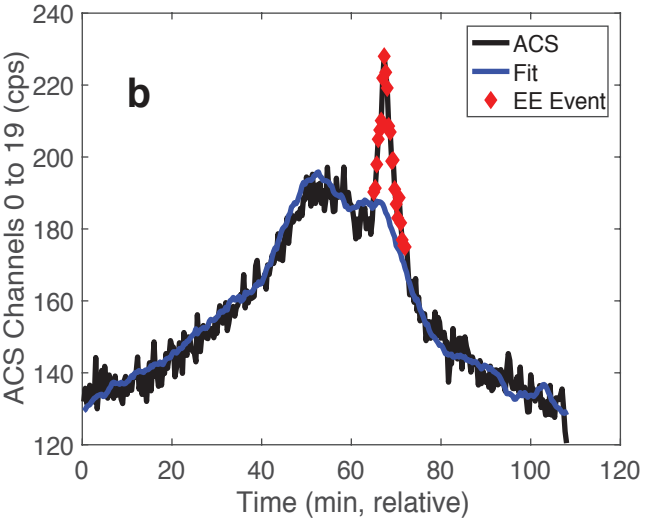

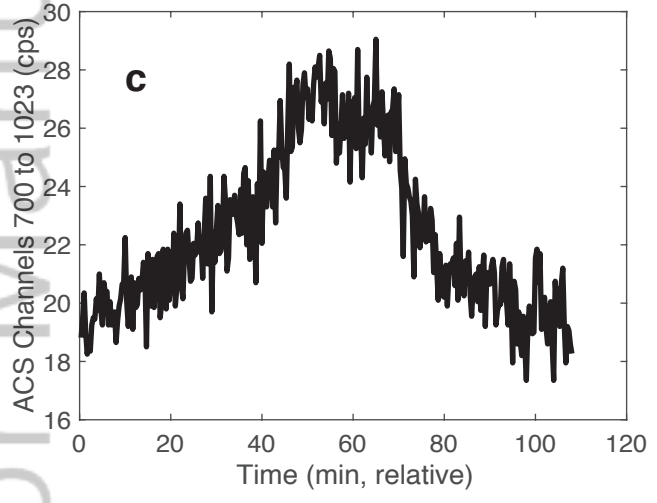

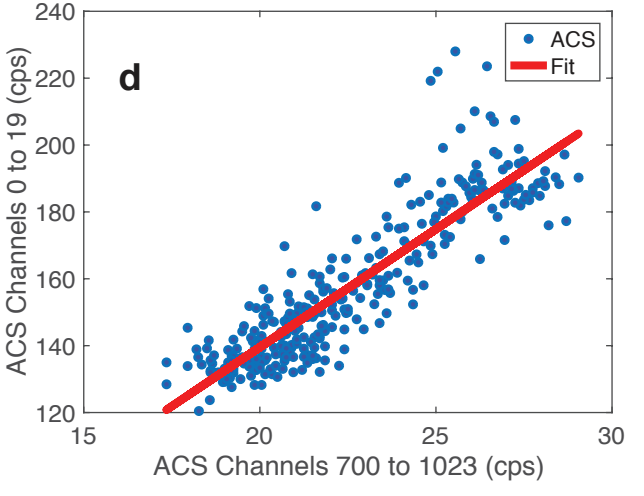

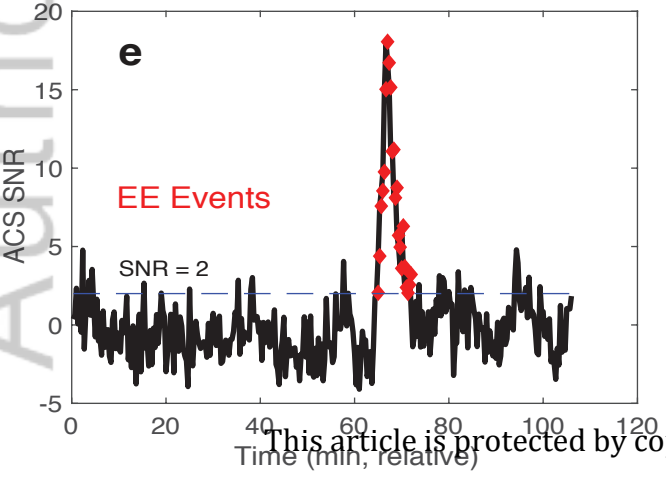

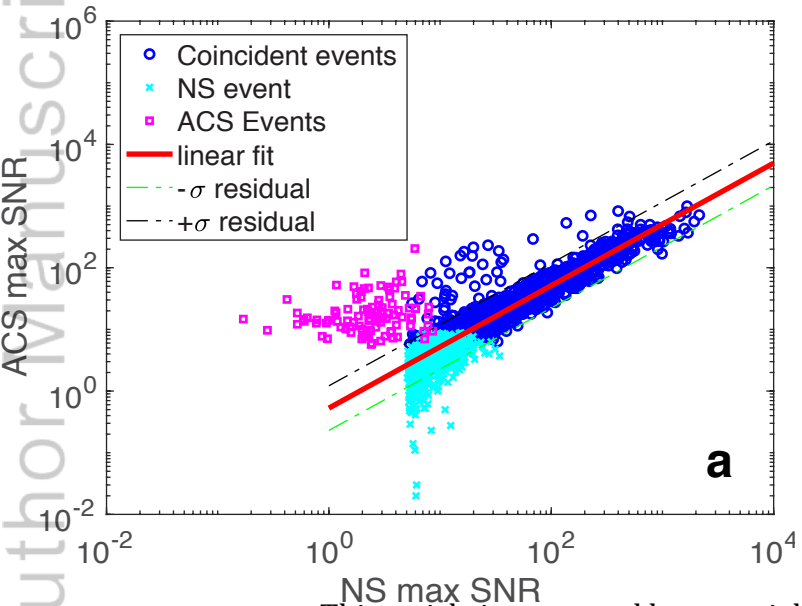

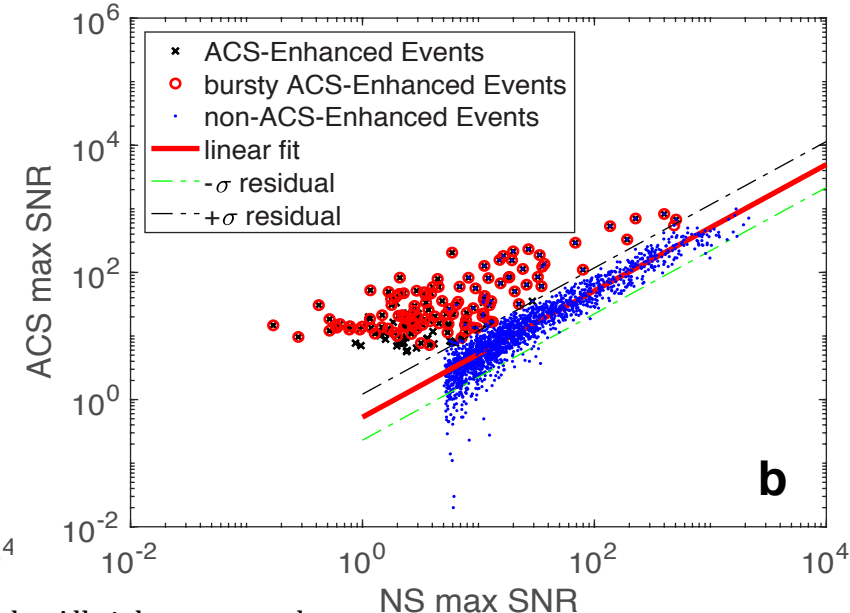

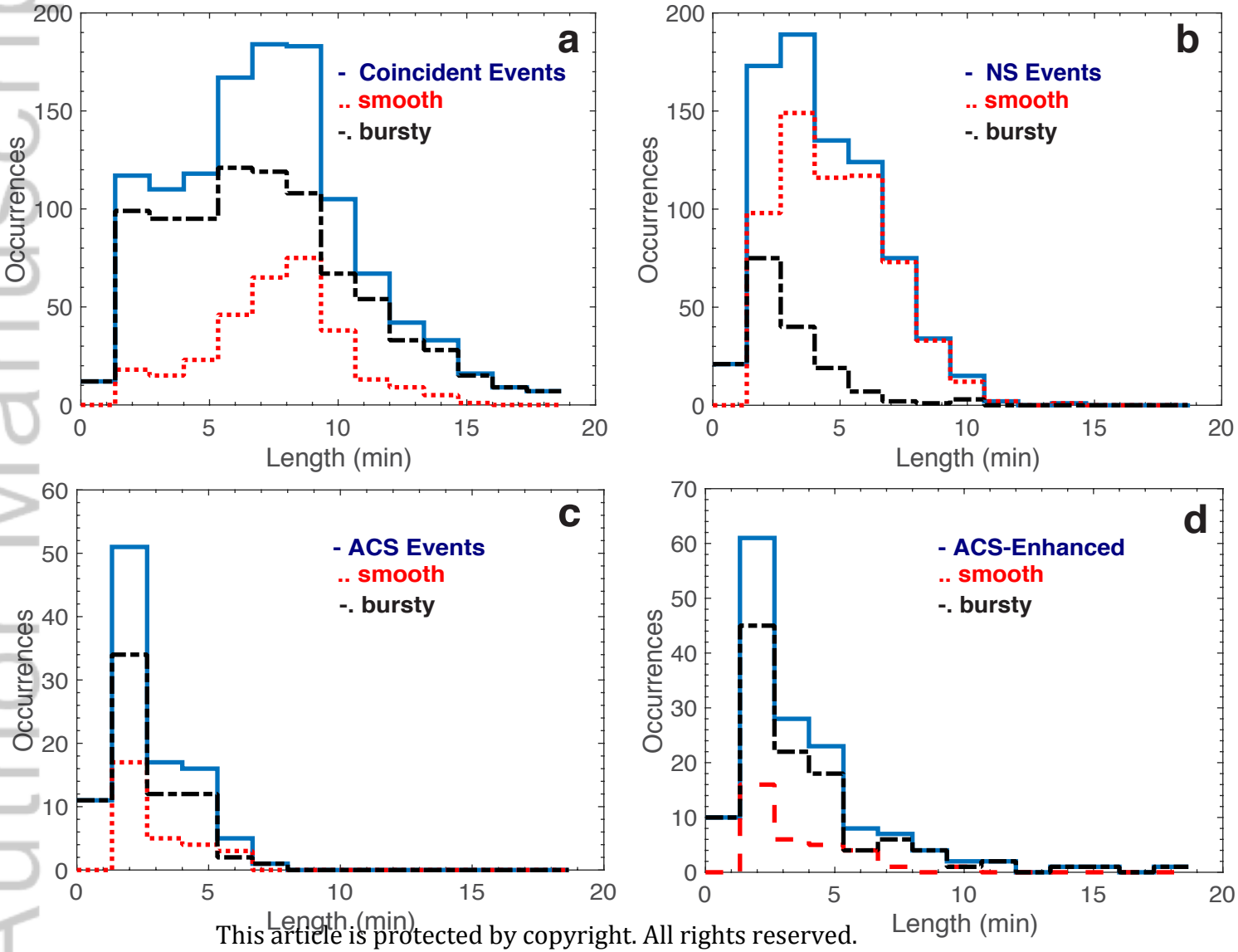

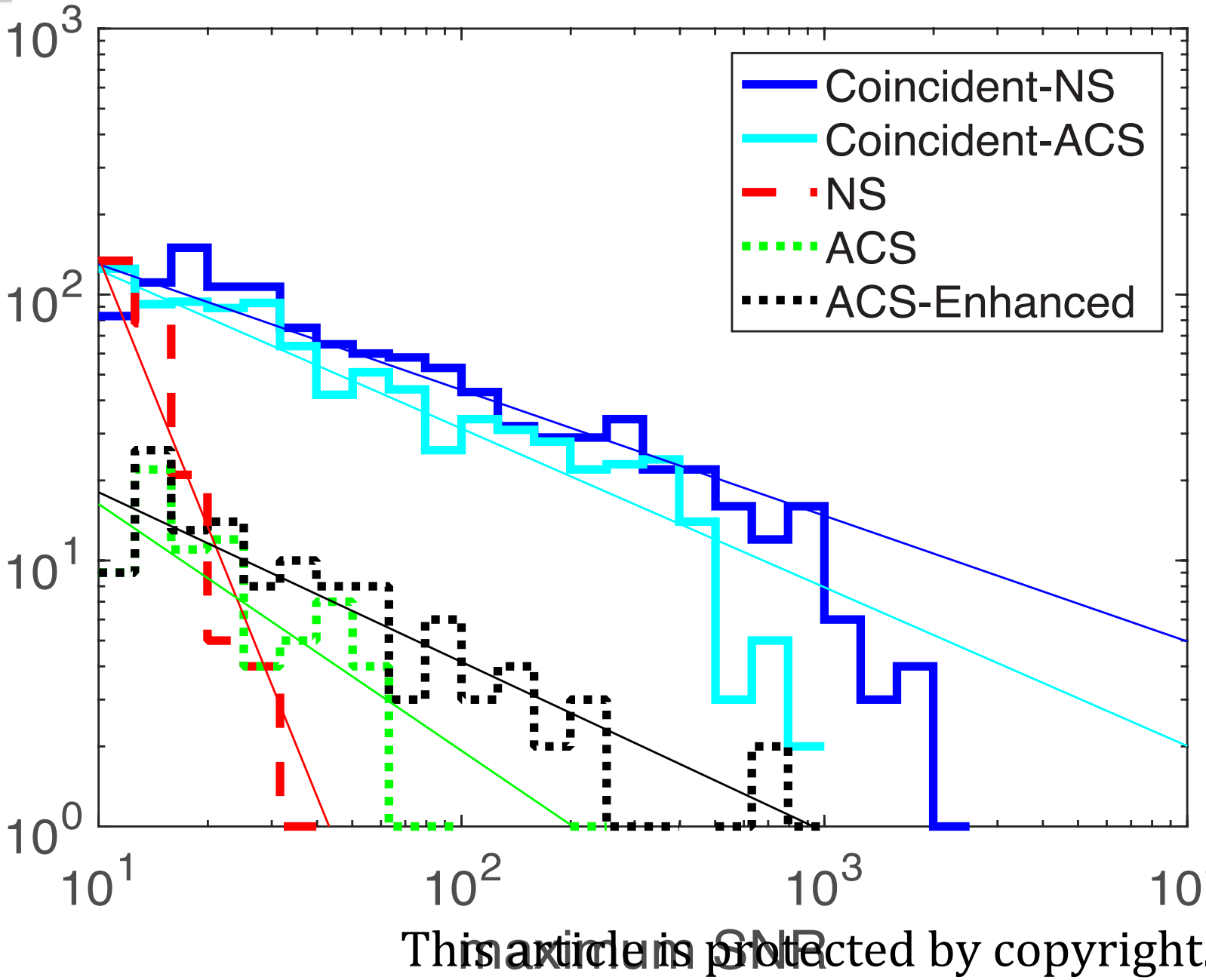

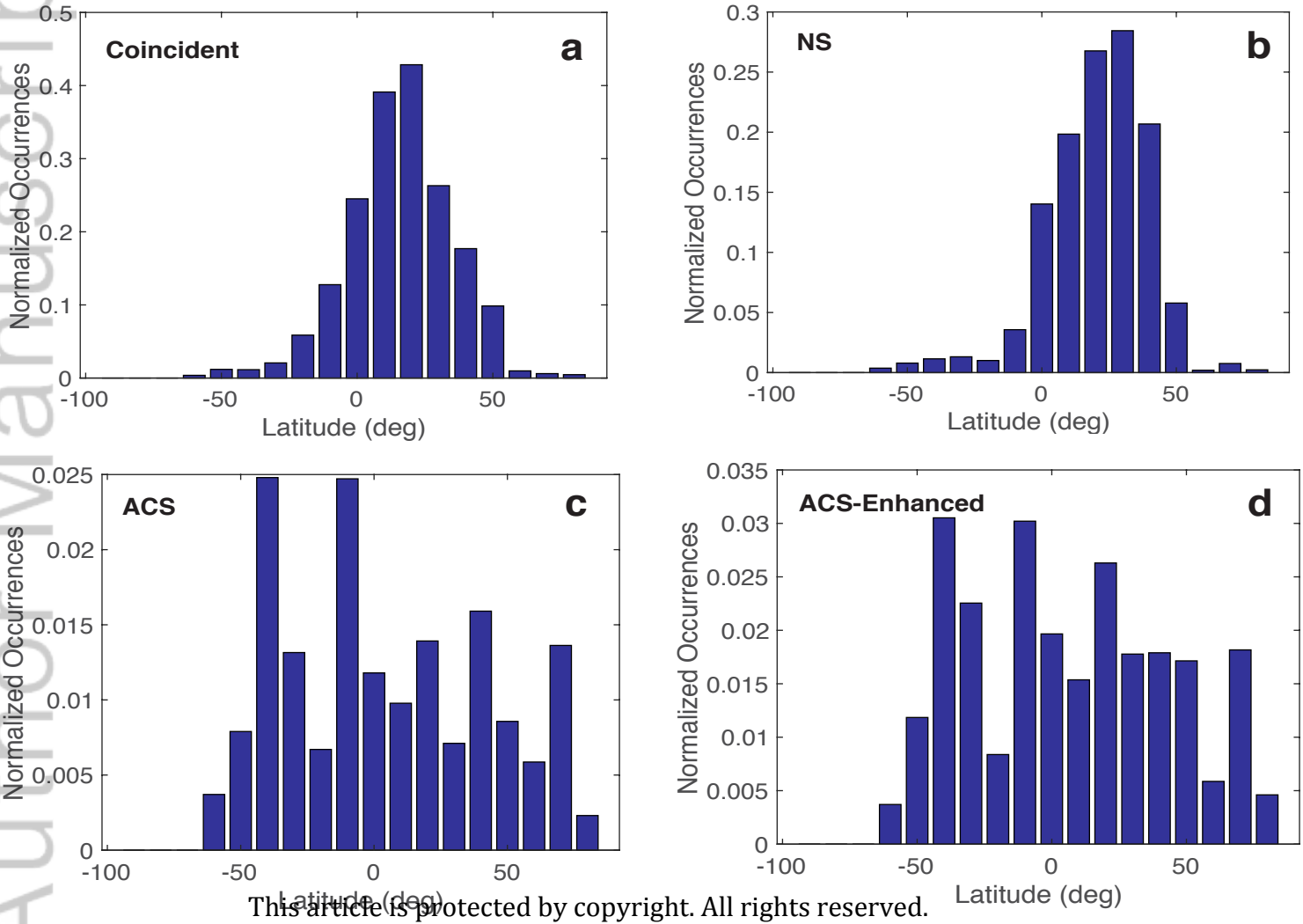

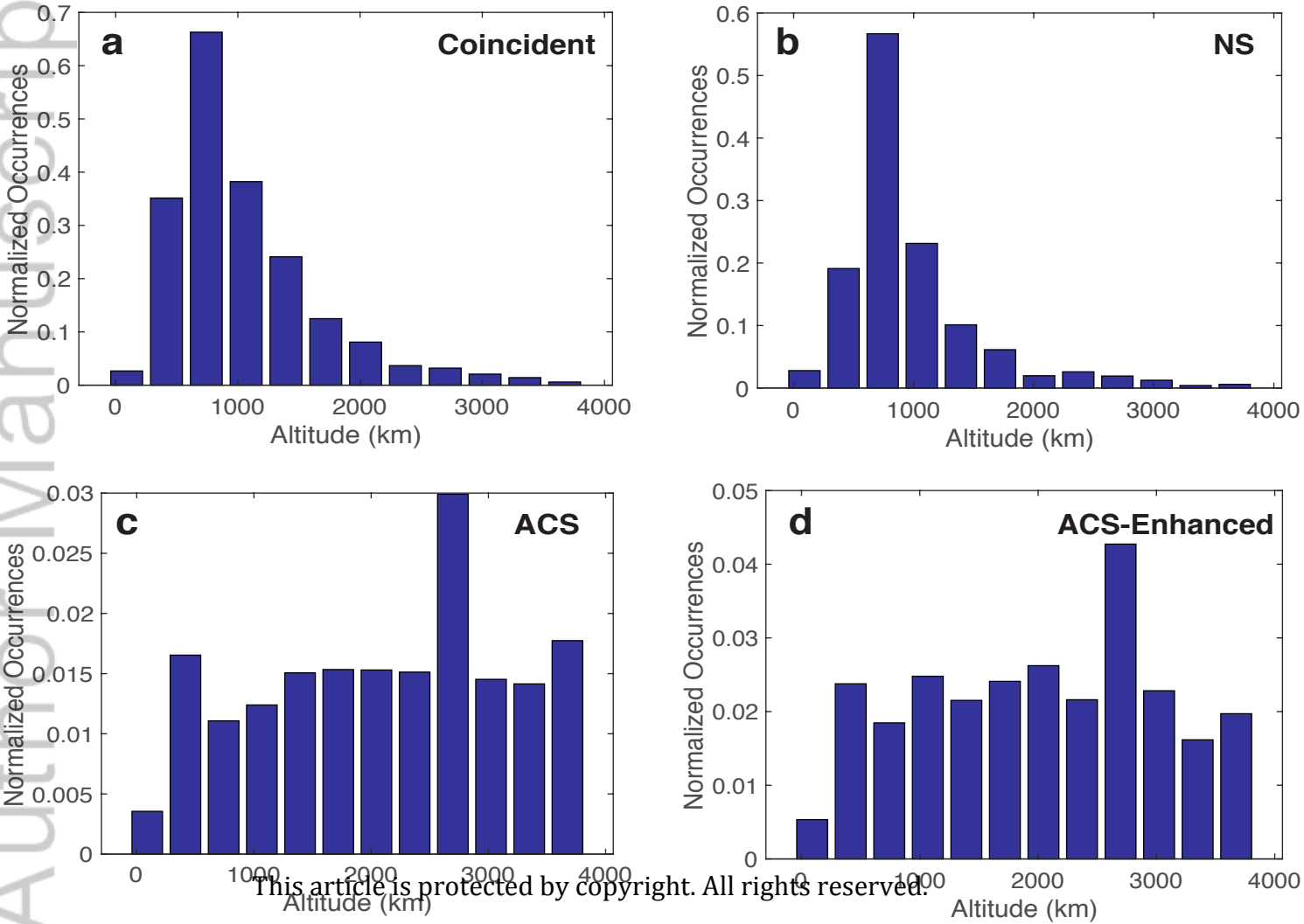

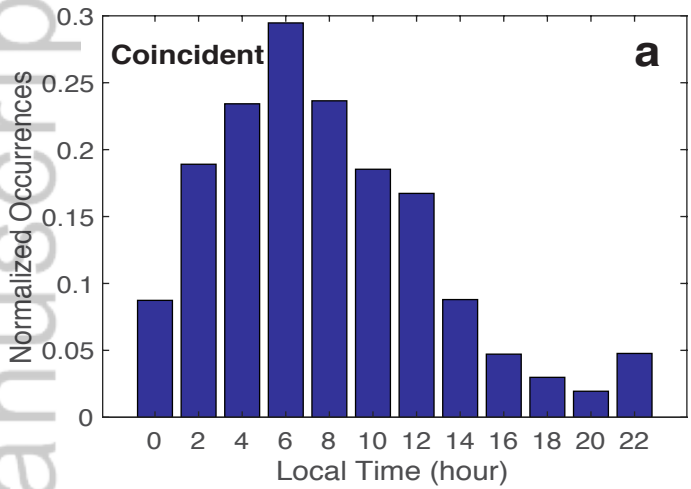

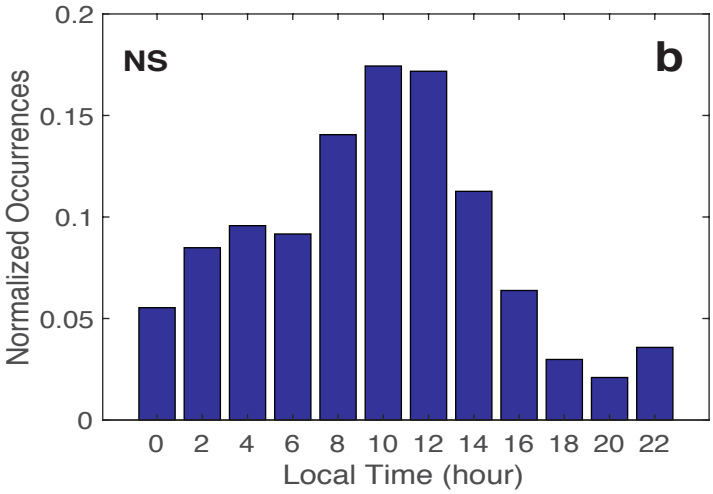

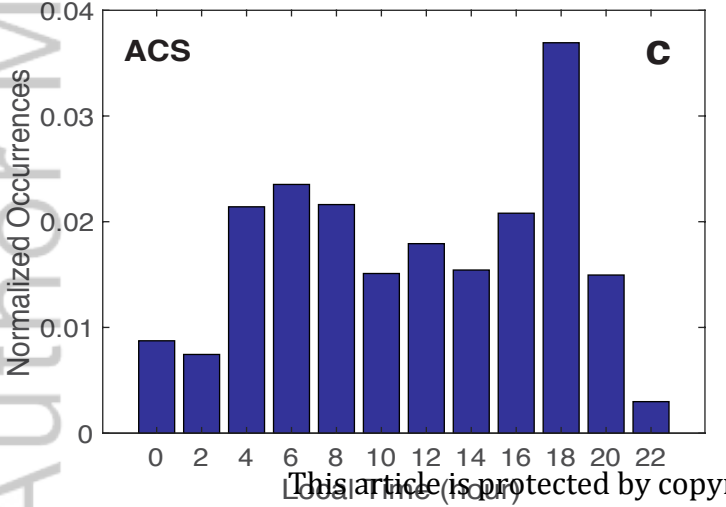

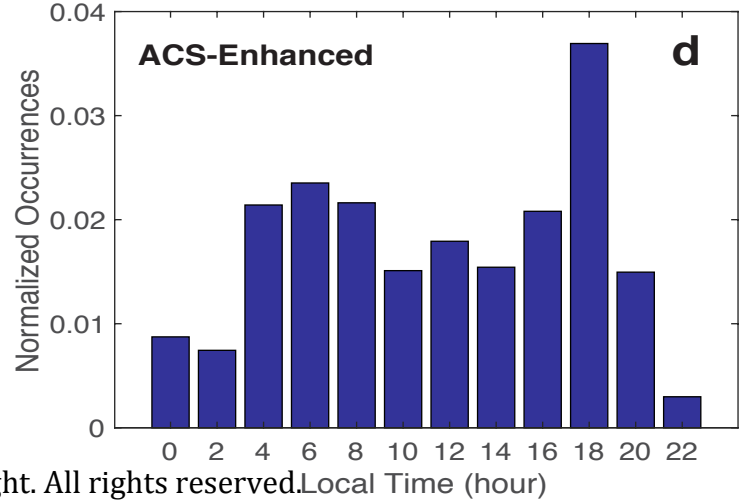

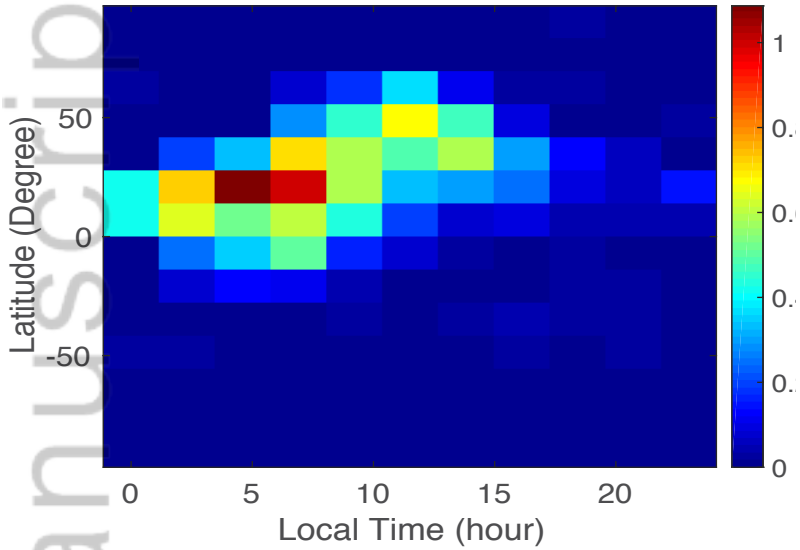

(a)

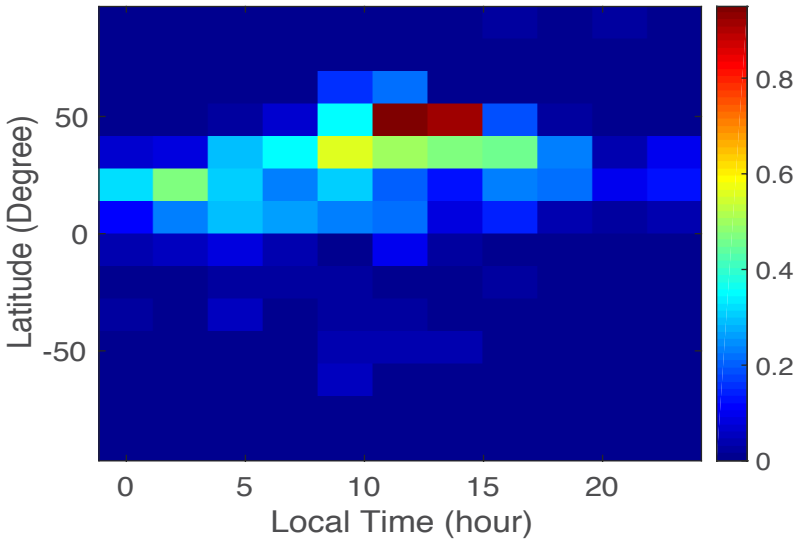

(b)

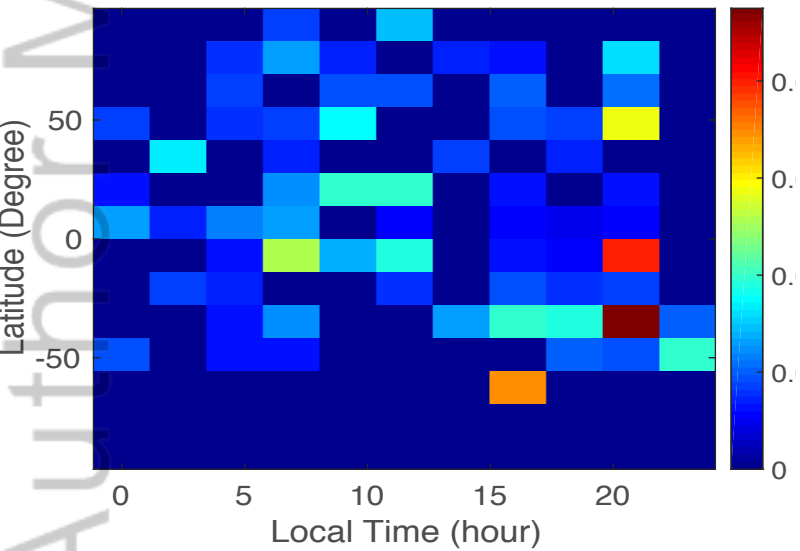

(c)

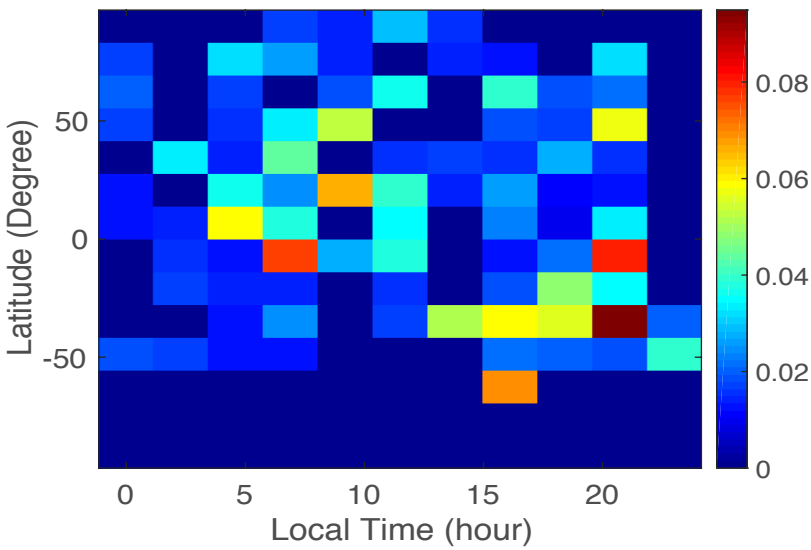

(d)